

LYMAS: PREDICTING LARGE-SCALE Ly α FOREST STATISTICS FROM THE DARK MATTER DENSITY FIELD

SÉBASTIEN PEIRANI¹, DAVID H. WEINBERG^{2,3}, STÉPHANE COLOMBI¹, JÉRÉMY BLAIZOT⁴, YOHAN DUBOIS¹, CHRISTOPHE PICHON¹

Submitted to the Astrophysical Journal

ABSTRACT

We describe LyMAS (Ly α Mass Association Scheme), a method of predicting clustering statistics in the Ly α forest on large scales from moderate resolution simulations of the dark matter distribution, with calibration from high-resolution hydrodynamic simulations of smaller volumes. We use the “Horizon MareNostrum” simulation, a $50 h^{-1}$ Mpc comoving volume evolved with the adaptive mesh hydrodynamic code RAMSES, to compute the conditional probability distribution $P(F_s|\delta_s)$ of the transmitted flux F_s , smoothed (1-dimensionally) over the spectral resolution scale, on the dark matter density contrast δ_s , smoothed (3-dimensionally) over a similar scale. In this study we adopt the spectral resolution of the SDSS-III Baryon Oscillation Spectroscopic Survey (BOSS) at $z = 2.5$, and we find optimal results for a dark matter smoothing length $\sigma = 0.3 h^{-1}$ Mpc (comoving). In its simplest form, LyMAS draws randomly from the hydro-calibrated $P(F_s|\delta_s)$ to convert dark matter skewers into Ly α forest pseudo-spectra, which are then used to compute cross-sightline flux statistics. In extended form, LyMAS exactly reproduces both the 1-dimensional power spectrum and 1-point flux distribution of the hydro simulation spectra. Applied to the MareNostrum dark matter field, LyMAS accurately predicts the 2-point conditional flux distribution and flux correlation function of the full hydro simulation for transverse sightline separations as small as $1 h^{-1}$ Mpc, including redshift-space distortion effects. It is substantially more accurate than a deterministic density-flux mapping (“Fluctuating Gunn-Peterson Approximation”), often used for large volume simulations of the forest. With the MareNostrum calibration, we apply LyMAS to 1024^3 N-body simulations of a $300 h^{-1}$ Mpc and $1.0 h^{-1}$ Gpc cube to produce large, publicly available catalogs of mock BOSS spectra^a that probe a large comoving volume. LyMAS will be a powerful tool for interpreting 3-d Ly α forest data, thereby transforming measurements from BOSS and other massive quasar absorption surveys into constraints on dark energy, dark matter, space geometry, and IGM physics.

Subject headings: large-scale structure of universe – quasars: absorption lines – intergalactic medium – methods: n-body simulations

1. INTRODUCTION

The Ly α forest – fluctuating absorption produced by intergalactic neutral hydrogen atoms in the spectra of background quasars – is the most powerful probe of cosmic structure at redshifts $z \approx 2 - 5$. The physics of Ly α forest absorption is relatively well understood, thanks to numerical simulations (e.g., Cen et al. 1994; Zhang, Anninos & Norman 1995; Hernquist et al. 1996; Miralda-Escudé et al. 1996 and related analytic methods (e.g., Bi & Davidsen 1997; Hui, Gnedin, & Zhang 1997) that accurately predict its statistical properties with minimal assumptions beyond those of the standard cosmological model. The power spectrum, correlation function, and probability distribution function (PDF) of Ly α forest flux have been used to constrain the underlying matter power spectrum and the thermal state of the intergalactic medium (IGM), with corresponding constraints on cosmological parameters and dark matter properties (e.g., Croft et al. 1998, 1999, 2002; McDonald et al. 2000, 2005; Zaldarriaga, Hui, & Tegmark

2001; Viel, Haehnelt, & Springel 2004; Seljak et al. 2005). These analyses have treated each sightline in isolation, as a collection of individual 1-dimensional tracks through the intergalactic gas distribution. The Baryon Oscillation Spectroscopic Survey (BOSS) of SDSS-III (Eisenstein et al. 2011; Dawson et al. 2013) is opening a new “3-dimensional” frontier in Ly α forest cosmology by measuring absorption on a grid of sightlines (150,000 quasars over 10,000 square degrees) that is large enough and dense enough to enable accurate measurements of transverse correlations across sightlines separated by tens of h^{-1} Mpc⁵. BOSS and potential successor surveys (e.g., BigBOSS, Schlegel et al. 2011) present a new theoretical challenge. For instance, the recent first measurements of Baryon Acoustic Oscillations (BAO) in the Ly α forest fluctuations in the BOSS Data Release 9 (Busca et al. 2012; Slosar et al. 2013) have opened new perspectives in constraining cosmological models, but the analysis and interpretation of such data require the development of efficient theoretical tools. In particular, to accurately predict the statistics of the Ly α forest at large scales for specified cosmological parameters, one must model physics on the pressure-support scale (a.k.a. the “Jeans scale”) of the IGM — about $0.1 - 0.3 h^{-1}$ Mpc for typical values and roughly $0.25 h^{-1}$ Mpc at overdensity of 10 (comoving at $z = 2 - 3$, see Peebles et al. 2010) — while simulating volumes many hundreds of h^{-1} Mpc on a side. This paper proposes and tests a new method of meeting this challenge.

⁵ Throughout the paper, we quote comoving distances in h^{-1} Mpc, where $h \equiv H_0/100 \text{ km s}^{-1} \text{ Mpc}^{-1}$.

¹ Institut d’Astrophysique de Paris (UMR 7095: CNRS & UPMC), 98 bis Bd Arago, 75014 Paris, France

² Department of Astronomy, The Ohio State University, Columbus, OH

³ Sorbonne Universités, Institut Lagrange de Paris (ILP), 98 bis Bd Arago, 75014 Paris, France

⁴ Université de Lyon, Lyon, F-69003, France; Université Lyon 1, Observatoire de Lyon, 9 avenue Charles André, Saint-Genis Laval, F-69230, France; CNRS, UMR 5574, Centre de Recherche Astrophysique de Lyon.

^a The LyMAS website can be found at: <http://www2.iap.fr/users/peirani/lymas/lymas.htm>



Most Ly α forest absorption arises in diffuse, highly photoionized gas, which is heated by photoionization and cooled adiabatically by expansion of the universe, leading to a tight correlation between temperature and density (Katz, Weinberg, & Hernquist 1996; Hui & Gnedin 1997). This correlation enables the Fluctuating Gunn-Peterson Approximation (FGPA; Weinberg, Katz, & Hernquist 1998; Croft et al. 1998), where the Ly α optical depth is tied to the local dark matter overdensity assuming photoionization equilibrium and the Gunn & Peterson (1965) formula for neutral hydrogen absorption. The FGPA can be applied to a log-normal density field created from Gaussian initial conditions (Gnedin & Hui 1996; Bi & Davidsen 1997) or to the dark matter density field of an N-body simulation, with pressure effects incorporated by smoothing the field at the gas Jeans scale or by using an approximate technique (Gnedin & Hui 1998) to incorporate pressure into the N-body evolution. Most efforts to systematically model large scale Ly α forest measurements and their dependence on cosmological parameters have used some variant of this approach, with full hydrodynamic simulations used to calibrate and test it (e.g., Croft et al. 1998, 1999, 2002; Zaldarriaga, Hui, & Tegmark 2001; McDonald et al. 2005). Growing computer power enables more ambitious approaches, and Viel, Haehnelt, & Springel (2006, 2010) used grids of hydrodynamic simulations to model Ly α forest statistics, but even these simulations ($60h^{-1}$ Mpc on a side) are tiny compared to the volume probed by BOSS.

There are several reasons that the N-body or log-normal approaches are unsatisfactory as a tool for modeling the 3-d Ly α forest. First, even without hydrodynamics, it is not currently feasible to model Gpc³ volumes while retaining good resolution on the gas Jeans scale. For example, even the heroic 3000³-particle simulations analyzed by Slosar et al. (2009) have an initial particle spacing of $0.5h^{-1}$ Mpc, while smoothed particle hydrodynamic (SPH) simulations require initial separations of $\sim 0.05h^{-1}$ Mpc to yield fully converged results (Lidz et al. 2010; Peebles et al. 2010). Second, the choice of smoothing scale for the dark matter inevitably produces some ambiguity in the predictions (Zaldarriaga, Hui, & Tegmark 2001); Ly α forest statistics are insensitive to this choice, but not perfectly so (Viel et al. 2002; Peebles et al. 2010). Third, the FGPA assumes a deterministic relation between dark matter overdensity and continuum-normalized Ly α flux ($F = e^{-\tau}$, hereafter simply “flux”), of the form $F = \exp[-A(\rho/\bar{\rho})^{2-0.6(\gamma-1)}]$, where $(\gamma-1)$ is the index of the gas temperature-density relation and A is a normalization constant that depends on several physical parameters (see Croft et al. 1998; Weinberg, Katz, & Hernquist 1998; Peebles et al. 2010). In practice, there is scatter around this relation because of peculiar velocities, shock heating of the gas above the temperature-density relation, and pressure-induced differences between the gas and dark matter distributions. Peculiar velocities, the largest source of scatter (Croft et al. 1997; Weinberg et al. 1999; Viel et al. 2002), can be incorporated into dark matter-based approaches, but the latter two effects require a hydrodynamic treatment. Finally, even if the FGPA were a perfect approximation on some scale (e.g., the gas Jeans scale), smoothing does not commute with the non-linear transformation between density and flux, so one cannot simply apply it to a lower resolution dark matter simulation and recover a lower resolution version of the transmitted Ly α flux.

We expect that the FGPA and log-normal methods, and even linear perturbation theory with effective bias factors calibrated on hydrodynamic simulations (McDonald 2003) are adequate on sufficiently large scales, e.g., for predicting the baryon acoustic oscillation (BAO) feature at $100h^{-1}$ Mpc (White 2003; McDonald & Eisenstein 2007; Slosar et al. 2009; White et al. 2010; Le Goff et al. 2011; Greig, Bolton & Wyithe 2011), which is the primary target of BOSS. Font-Ribera, McDonald & Miralda-Escudé (2012) have developed an efficient semi-analytic method for generating mock data sets for the large-scale Ly α forest, tailored to reproduce the observed power spectrum and PDF, which allows tests for systematics in analysis methods and calculation of statistical errors and covariance matrices. But BOSS and other 3-d Ly α forest surveys will also enable precise measurements of flux correlations at scales of a few h^{-1} Mpc to a few tens of h^{-1} Mpc, where these approximations may not be accurate relative to the measurement precision. Large simulation volumes are still needed in this regime, both to eliminate systematic effects of the finite box size and to ensure that statistics are limited by the available data not by the available simulation volume. Deriving constraints and error bars requires making predictions as a function of cosmological and IGM parameters. Angulo & White (2010) have proposed an elegant and accurate method for remapping non-linear dark matter distributions from one cosmology to another, so these parameter explorations can be kept inexpensive if one can carry them out with moderate resolution N-body simulations.

In this paper, we make explicit the separation-of-scale philosophy that is already implicit in these alternative methods to predict large-scale Ly α forest statistics. We concentrate on the conditional flux probability distribution (PDF), the probability $P(F_2|F_1, \Delta r_p, \Delta r_z)$ of finding flux $F_2 = e^{-\tau_2}$ in a spectral pixel at location 2 given that the flux has the value F_1 in a pixel with transverse (projected) separation Δr_p (see Miralda-Escudé et al. 1997). Other two-point statistics such as the flux correlation function $\langle (F_2 - \bar{F})(F_1 - \bar{F}) \rangle$ can be computed by integrating over this distribution and the unconditional PDF (see §3). It seems reasonable in principle that to predict this distribution on large scales we should only need to resolve the matter distribution on scales $r_{\text{res}} \ll [(\Delta r_p)^2 + (\Delta r_z)^2]^{1/2}$. High-resolution hydrodynamic simulations are needed to compute the relation between the flux F_s , smoothed (1-dimensionally) on the scale of instrumental resolution or some deliberately chosen larger scale, and the matter density contrast δ_s , smoothed (3-dimensionally) on a scale larger than the simulation resolution but smaller than the separations being probed. For the reasons discussed above, this relation is not deterministic but stochastic, described by a conditional probability distribution $P(F_s|\delta_s)$.

Our conjecture is that one can predict $P(F_{s,2}|F_{s,1}, \Delta r_p, \Delta r_z)$ for a given cosmological and IGM model by using a moderate resolution N-body simulation to compute $P(\delta_{s,2}|\delta_{s,1}, \Delta r_p, \Delta r_z)$ and convolving this with the local conditional distribution computed from high-resolution hydro simulations, $P(F_s|\delta_s)$ evaluated for $\delta_{s,1}$ and $\delta_{s,2}$. Physically, we are assuming that the fluxes at positions 1 and 2 are correlated because the matter densities at these positions are correlated, and that the *deviation* $F_{s,2} - \langle F_s|\delta_{s,2} \rangle$ from the conditional mean is uncorrelated with the *deviation* $F_{s,1} - \langle F_s|\delta_{s,1} \rangle$. The assumption of uncorrelated deviations will certainly fail for closely neighboring pixels, whose fluxes will lie above or below the conditional mean for the same reason, but we expect it to be

come accurate quickly at larger separations.

We test this conjecture explicitly using a large, adaptive mesh refinement (AMR) simulation of a $50h^{-1}$ Mpc comoving volume, realized with 1024^3 dark matter particles and a 1024^3 top-level hydro grid, evolved with the AMR hydro code RAMSES (Teyssier 2002). We use this simulation to calibrate the $P(F_s|\delta_s)$ relation for several choices of dark matter and Ly α smoothing scales. We then compare the Ly α forest statistics computed from the gas distribution of the simulation to those computed from the dark matter distribution by the procedure described above, which we refer to as LyMAS for Ly α Mass Association Scheme⁶. We also compare results to the deterministic FGPA approach applied on the same smoothing scales, finding that LyMAS is significantly more accurate at small separations. For compactness, we will sometimes abbreviate Ly α forest to Ly α F in the remainder of the paper.

In the next section we describe the hydro simulation and our methods for creating Ly α F spectra and for extracting skewers of the smoothed dark matter density field. Section 3 presents LyMAS in its simplest form, which is designed to predict flux statistics across sightlines but does not produce realistic artificial spectra, because it ignores correlated deviations of $F_s - \langle F_s|\delta_s \rangle$ along an individual line of sight. In §4 we describe an extended scheme that produces artificial spectra with a 1-d flux power spectrum and 1-point PDF that (almost) exactly match those of the full spectra from the hydro simulation while retaining the accurate performance of LyMAS for cross-sightline statistics. In §5 we describe the application of LyMAS to N-body simulations of a $300h^{-1}$ Mpc and $1.0h^{-1}$ Gpc comoving volume, illustrating the impact of finite box size on flux correlation statistics. We summarize our results and look towards future applications in §6. Finally, in the website dedicated to LyMAS, we describe several sets of electronic tables being made available with this paper, presenting the conditional flux PDFs computed from the MareNostrum hydro simulation and the mock spectra extracted from the large N-body simulations.

2. HYDRODYNAMIC SIMULATION AND CREATION OF SPECTRA

In this section, we introduce the “Horizon-MareNostrum” simulation, a high resolution cosmological N-body and hydrodynamics simulation we have analyzed to generate our calibrations. We will then describe our procedures to extract from this simulation the Ly α F spectra as well as DM density fields.

2.1. The “Horizon-MareNostrum” simulation

The Horizon-MareNostrum simulation (which we hereafter refer to simply as MareNostrum) was run for a Λ CDM universe using WMAP1 parameters (Spergel et al. 2003), namely $\Omega_M = 0.3$, $\Omega_\Lambda = 0.7$, $\Omega_B = 0.045$, $H_0 = 70.0$ km/s/Mpc, $n = 1$ and $\sigma_8 = 0.9$. The simulation was performed in a periodic box of side $50h^{-1}$ Mpc with 1024^3 dark matter particles (e.g. with mass resolution of $\sim 1.41 \times 10^7 M_\odot$) and an adaptive mesh refinement (AMR) technique (Teyssier 2002) was used to keep the spatial resolution fixed at $\sim 1h^{-1}$ kpc in physical units. The evolution of the thermodynamic properties of the gas depends on a wide range of physical processes. In particular,

⁶ French readers may appreciate the resonance with MoLUSC (Sousbie, Courtois, Bryan, & Devriendt 2008), which utilizes a similar style of dual-level calculation to predict large scale galaxy clustering.

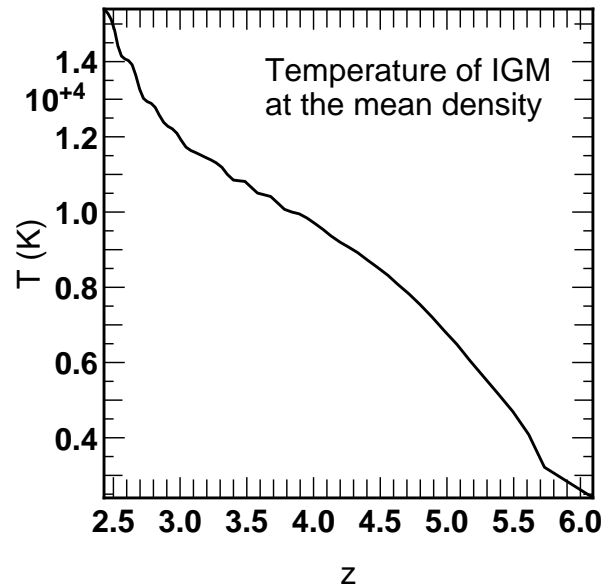


FIG. 1.— Evolution of the mean temperature of the IGM at the mean density from redshift 6.5 to 2.5 in the MareNostrum simulation. The mean temperature of the IGM tends to increase as a function of time mainly due to the global action of UV background, supernovae feedback and shock-heating of the gas during galaxy formation processes.

MareNostrum incorporates metal-dependent cooling and photoionization heating from a UV background computed via the prescriptions of Haardt & Madau (1996), starting at a reionization redshift $z = 8.5$. A model of supernova feedback and metal enrichment has also been incorporated using the implementation described by Dubois & Teyssier (2008). The high-redshift Ly α forest arises mainly in gas with overdensity $1 + \delta \lesssim 50$, whose thermal evolution is governed primarily by photoionization heating and adiabatic cooling from the expansion of the universe. For reference, Figure 1 shows the evolution of the mean temperature of the IGM at the mean density (from $z = 6.5$ to $z = 2.5$), and Figure 2 shows the mass-weighted temperature-density diagram of the MareNostrum simulation at our analysis redshift $z = 2.51$. At densities $n \leq 10^{-4} \text{ cm}^{-3}$ one sees the usual sharp locus of photoionized gas, with a small fraction of gas shock heated above this relation. At higher densities one sees shock-heated gas in halos and the locus of radiatively cooled and star-forming gas in galaxies. For further details of the MN simulation, we refer the readers to previous papers that have used it for other analyses (Ocvirk et al. 2008; Devriendt et al. 2010).

2.2. Extracting Ly α F spectra

We compute Ly α absorption spectra along about one million lines of sight cast through the $z = 2.51$ output of the MareNostrum simulation. At this redshift, the simulated volume allows us to probe Ly α absorption lines over a range of $\sim 75\text{\AA}$ around the observed wavelength $\lambda \sim 4268\text{\AA}$. For a given sight-line, the opacity at observer-frame frequency ν_{obs} is $\tau(\nu_{obs}) = \sum_{\text{cells}} n_{\text{HI}} \sigma(\nu_{obs}) dl$, where the sum extends over all (leaf) cells traversed by the ray⁷, n_{HI} is the numerical density of neutral H atoms in each cell, $\sigma(\nu_{obs})$ is the cross section of Hydrogen to Ly α photons, and dl is the physical cell size. We

⁷ In practice, we actually extend this sum further by replicating the periodic simulated volume at both ends of the rays.

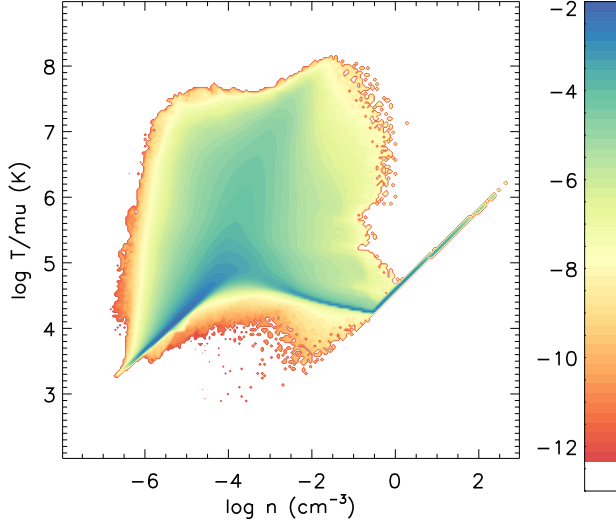


FIG. 2.— Mass-weighted Temperature-density diagram of the MareNostrum simulation at $z = 2.51$. The mean density of the baryons is at $\bar{n} \simeq 10^{-5} \text{ cm}^{-3}$ at this redshift.

compute $\sigma(\nu_{obs})$ as:

$$\sigma(\nu_{obs}) = f_{12} \frac{\pi e^2}{m_e c} \times \frac{H(a, x)}{\sqrt{\pi} \Delta \nu_D}, \quad (1)$$

where $f_{12} = 0.4162$ is the Ly α oscillator strength, e and m_e are the electron’s charge and mass, $\Delta \nu_D = (2k_B T / m_H)^{1/2} \times \nu_\alpha / c$ is the Doppler frequency width due to thermal motions of atoms at temperature T , and $a = \Delta \nu_L / (2\Delta \nu_D)$ is the ratio of the natural line width ($\Delta \nu_L \sim 9.9 \cdot 10^7 \text{ s}^{-1}$) to the Doppler frequency width. The cross section is a function of frequency in the rest-frame of the absorbing gas cell $\nu_{cell} = \nu_{obs}(1+z)(1+v/c)$ (where v is the cell’s line-of-sight velocity), which we use to define the dimensionless frequency offset $x = (\nu_{cell} - \nu_\alpha) / \Delta \nu_D$. Finally, the Hjerting function $H(a, x)$ is:

$$H(a, x) = \frac{a}{\pi} \int_{-\infty}^{\infty} \frac{e^{-y^2} dy}{a^2 + (x-y)^2}. \quad (2)$$

In practice, for each sight-line, we compute the opacity due to all cells on a high-resolution grid of observer-frame wavelength (with $d\lambda = 0.02 \text{ \AA}$). We then compute a high-resolution normalized flux $F(\lambda) = \exp(-\tau)$, which we integrate down to the targeted 1024 λ -bins. At the observed frame wavelength $\lambda_{Ly\alpha}(1+z) = 4268 \text{ \AA}$, the resolution of the BOSS spectrographs (Eisenstein et al. 2011; Smee et al. 2012) is $\lambda/\Delta\lambda \approx 1740$, where $\Delta\lambda$ is the FWHM of the line-spread function, implying $\Delta\lambda = 2.46 \text{ \AA}$. The corresponding Gaussian dispersion is $\sigma = \Delta\lambda / (2\sqrt{2 \ln 2}) = 1.045 \text{ \AA}$, which translates to a comoving distance of $0.696 h^{-1} \text{ Mpc}$. To mimic the effects of BOSS spectral resolution, therefore, we convolve our extracted Ly α F spectra with a 1-d Gaussian of dispersion $\sigma = 0.696 h^{-1} \text{ Mpc}$.

Note also that when generating our grid of flux, the MareNostrum simulation leads to a mean flux decrement with a slightly too high value. Following standard practice in Ly α forest modeling, we match the observed mean

decrement at $z \sim 2.5$ (Faucher-Giguère et al. 2008) by changing the UV background intensity in post-processing, increasing its intensity by a factor of about 1.3. The results should be virtually identical to those of a simulation run with this higher intensity background during evolution, since at IGM densities the photoionization heating rate is insensitive to the UV background intensity (Thoul & Weinberg 1996; Katz, Weinberg, & Hernquist 1996).

2.3. Extracting dark matter skewers

To extract dark matter skewers, we follow a 3-step process:

- Adaptive interpolation of the DM particle distribution on a high resolution grid (here a 1024^3 grid for the Horizon-MareNostrum simulation and a 4096^3 grid for the GADGET simulations of Section 5). Note that this interpolation is performed after projection into redshift space if needed. Redshift space projection is performed along the z coordinate, so that we work in the distant observer limit.
- Smoothing with a Gaussian window in Fourier space, using the fact that even when working in redshift space, periodicity of the box is preserved because we use the distant observer limit.
- Extraction of the skewers from a grid of lines of sight aligned along the z axis and positioned at random otherwise.

The adaptive interpolation method we use is described by Colombi, Chodorowski & Teyssier (2007), so we give here only a quick sketch of it. It is similar to SPH interpolation except that it is not a direct projection of the particles as an ensemble of round clouds on the grid. Indeed, the SPH interpolation method, if used as is, can behave poorly in underdense regions, where it can leave totally empty grid sites. To avoid this defect, each grid site is considered as a virtual particle and the N_{SPH} closest particles to it are found (here $N_{\text{SPH}} = 32$). Then we perform a calculation of the density at the center of the cell using a weight for each particle i that is roughly proportional to $W(r_i)$, where r_i is the distance of the particle to the center of the cell and where $W(r)$ is a standard SPH kernel function (Monaghan 1992). We use the term “roughly” because the actual interpolation scheme is more complex than that: (i) special treatment is performed when the number of particles in the cell, N_p , exceeds N_{SPH} : in this case, we perform the interpolation over the N_p particles instead of N_{SPH} : this is to minimize the deviation from total mass conservation discussed below; (ii) to make sure that the total contribution of each particle equals its mass m , a renormalization of its local contribution to each cell is performed *a posteriori* (i.e., after calculating its contribution to each individual cell). Our scheme does not guarantee that all the particles contribute: there might be some cases where a particle could not contribute to any grid site, which means that the total mass is not conserved exactly. This effect is however small, usually of the order of 0.1 percent (it is fixed by an overall renormalization of the grid density).

The adaptive interpolation scheme is relatively expensive, but it preserves high-resolution information in overdense regions of the dark matter field. We have not tested LyMAS with simpler density assignment methods such as cloud-in-cell, so we caution that our favorable findings below might not apply in this case.

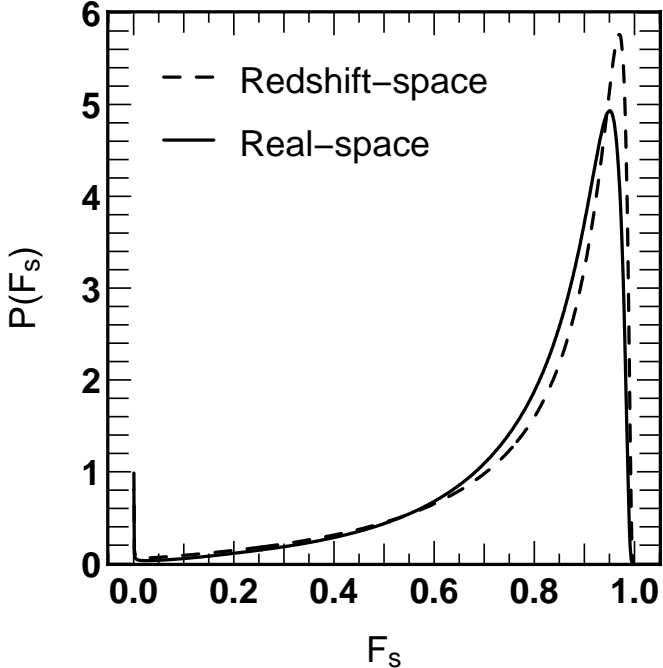


FIG. 3.— Unconditional PDF of the spectra extracted from the hydro simulation at redshift $z = 2.51$, in real space (solid) and redshift space (dashed). The effective optical depth $\tau_{\text{eff}} = -\ln F_s$ is 0.2301 and 0.2288 for real and redshift space, respectively, in good agreement with the observational estimate of Faucher-Giguère et al. (2008) at $z = 2.5$. Spectra have been smoothed with a Gaussian of $\sigma = 0.696 h^{-1} \text{Mpc}$ (comoving) to mimic BOSS spectral resolution.

3. PREDICTING CONDITIONAL FLUX DISTRIBUTIONS

Our approach to predicting Ly α F flux statistics is based on the conditional distribution of flux given density. Figure 3 plots the *unconditional* flux PDF of the Ly α F spectra extracted from the hydro simulation, in real space and in redshift space, where the spectra have been smoothed to BOSS resolution. Figure 4 plots contours of the joint distribution of optical depth $\tau_s = -\ln F_s$ and overdensity $(1 + \delta_s)$, where the subscript s emphasizes that the flux is smoothed (in one dimension) to the BOSS spectral resolution and the density contrast is smoothed with a 3-d Gaussian of radius $\sigma = 0.3 h^{-1} \text{Mpc}$ (top panels) or $1.0 h^{-1} \text{Mpc}$ (bottom panels). The top left panel shows a tight correlation between the real space smoothed overdensity and the “real space” Ly α F flux, i.e., the flux computed with all gas peculiar velocities (but not thermal broadening) set to zero. This tight correlation, first noted by Croft et al. (1997), provided the initial motivation for the FGPA. Croft et al. noted that the scatter in the correlation goes up when one includes peculiar velocities of the gas, which shift the line of sight location of absorption features and raise or lower optical depths through convergence or divergence in velocity space. We see this effect in the top middle panel of Figure 4. However, in the right panels we show the correlation when the dark matter distribution is *also* computed in redshift space: the scatter decreases, producing a correlation that is essentially just as tight as the one obtained in real space.

The same trends hold for a $1.0 h^{-1} \text{Mpc}$ smoothing length (lower panels), but in this case the range of densities is compressed, and the correlation is steeper. As a result, the scat-

ter in optical depth has larger impact relative to the trend with density. For our calculations below, we have experimented with a range of smoothing lengths, and we find that the best results (i.e., the most accurate predictions for flux statistics) are obtained with a smoothing length in the range $\sim 0.2 - 0.35 h^{-1} \text{Mpc}$. This is comparable to the Jeans scale for $1 + \delta = 10$ (Peebles et al. 2010) and somewhat smaller than the BOSS spectra resolution scale of $\sigma = 0.696 h^{-1} \text{Mpc}$. We have not tested whether smaller smoothing lengths would give better results for higher resolution spectra. However, we also carry out most of our tests for $1.0 h^{-1} \text{Mpc}$ smoothing, as this still works quite well, and it can be applied to N-body simulations with lower resolution.

The FGPA converts DM density to optical depth using a physical model motivated by photoionization equilibrium assuming that all gas contributing to the Ly α F lies on a temperature-density relation $T \propto (\rho/\bar{\rho})^{\gamma-1}$, leading to $\tau \propto (\rho/\bar{\rho})^{2-0.7(\gamma-1)}$. This relation makes sense for modeling high-resolution spectra, but it does not necessarily apply at low resolution because of the non-linear relation between flux and optical depth, and even in the high-resolution case it omits some physical effects. Alternatively, one can derive an “optimal” deterministic relation between smoothed density and smoothed flux that is calibrated on hydro simulations, a strategy advocated by Gallerani et al. (2011). A straightforward choice for an “optimal” mapping is to find the unique monotonic relation between the smoothed matter density and the smoothed flux such that the spectra generated from the dark matter have the same unconditional 1-point flux PDF as the spectra from the hydro simulation. We do so by matching the corresponding cumulative distributions to a pixel with DM contrast δ_s we assign a flux F_s such that

$$\int_0^{F_s} P(F'_s) dF'_s = \int_{\delta_s}^{\infty} P(\delta'_s) d\delta'_s, \quad (3)$$

where $P(F_s)$ and $P(\delta_s)$ are the 1-point PDFs of flux and DM density measured from the simulation. Figure 5 illustrates this procedure graphically and shows the resulting mapping, which is slightly different in real space and redshift space because the PDFs are different in the two cases (see Fig. 3). The mapping is also different if we consider the $1.0 h^{-1} \text{Mpc}$ DM smoothing rather than the $0.3 h^{-1} \text{Mpc}$ smoothing. Well after reionization, the interplay between photoionization heating and adiabatic cooling produces a temperature-density relation $T \propto \rho^{0.6}$ in the diffuse photo-ionized medium that dominates the Ly α F (Katz, Weinberg, & Hernquist 1996; Hui & Gnedin 1997), and in this case (which applies in our simulation) the FGPA predicts $\tau \propto \rho^{1.6}$. Our deterministic relations for $0.3 h^{-1} \text{Mpc}$ smoothing have this logarithmic slope at low density, but the relation flattens somewhat at higher density, with lower optical depth than the $(1 + \delta_s)^{1.6}$ extrapolation predicts. This flattening may be partly a consequence of working at BOSS resolution rather than high resolution. We will use the deterministic mappings plotted here as a foil for evaluating the success of the LyMAS probabilistic scheme.

The scatter in Figure 4 shows that the relation between DM density and flux is not, in fact, deterministic. Figure 6 plots the conditional probability distributions $P(F_s|\delta_s)$ for dark matter density contrasts $\delta_s = -0.5, 0, 1, \text{ and } 4$; each curve represents a vertical cut through the corresponding panel of Figure 4. Beginning with the top row, for DM smoothing length $\sigma = 0.3 h^{-1} \text{Mpc}$, we see that these conditional distribu-

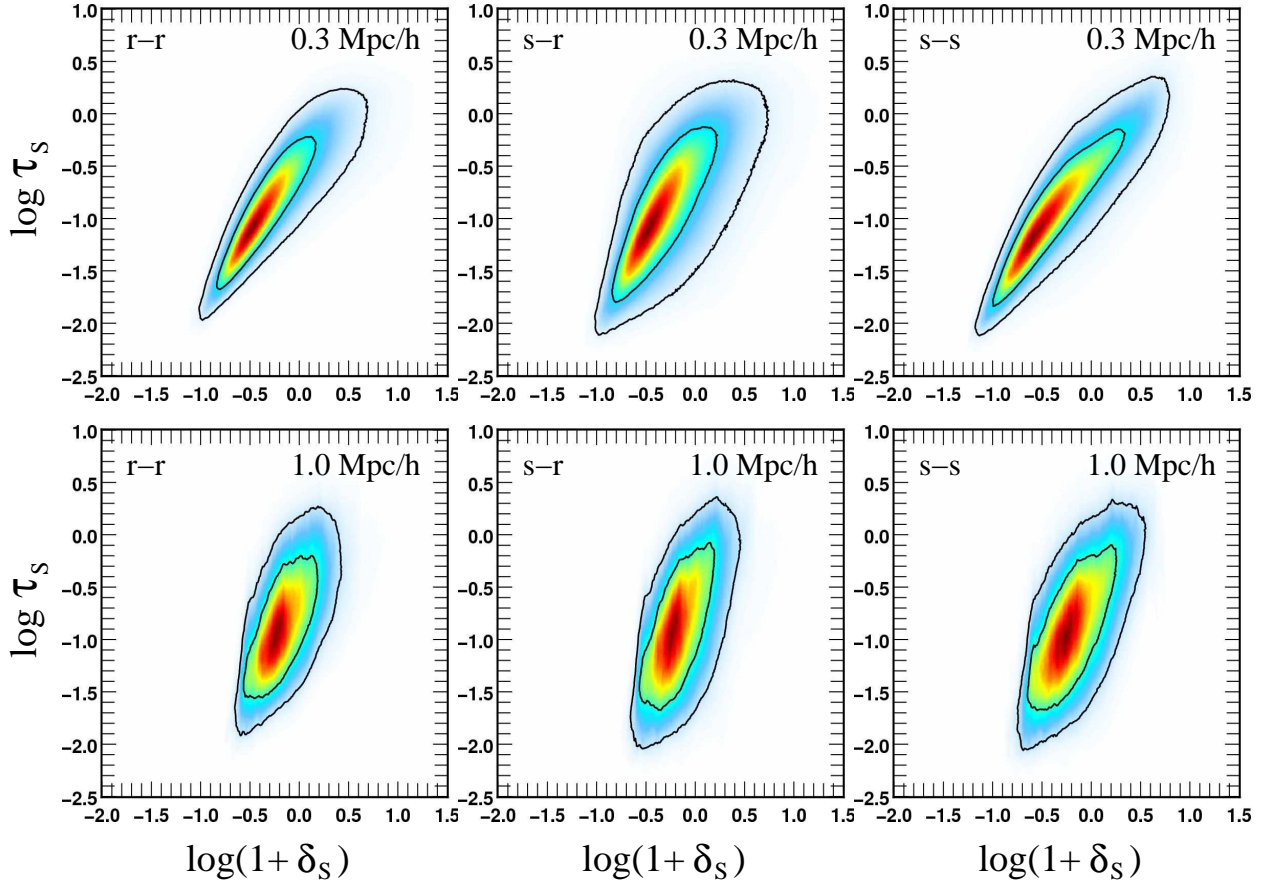


FIG. 4.— Correlation between optical depth $\tau_s = -\ln F_s$ in the hydro spectra and the smoothed DM overdensity $(1 + \delta_s)$ at the same location along the line of sight, for comoving DM smoothing lengths of $0.30 h^{-1}$ Mpc (top row) and $1.0 h^{-1}$ Mpc (bottom row). Colors show the density of pixels in the $\log \tau_s - \log(1 + \delta_s)$ plane, and contour lines mark areas enclosing 68.27% 95.45% respectively. Left panels show the case with spectra and DM density both computed in real space (peculiar velocities set to zero), middle panels show redshift space spectra and real space density, and right panels show both computed in redshift space.

tions are quite broad, though they always show the expected trend of lower average flux for higher DM density. The middle panel, based on redshift-space spectra but real-space DM densities, has broader distributions as expected. However, when we use redshift-space DM densities (right panel), the distributions are if anything sharper and more differentiated than those obtained for real-space spectra and real-space DM densities (left panel). The bottom row, for DM smoothing $\sigma = 1.0 h^{-1}$ Mpc, shows similar trends, but the curves are less differentiated than those for $\sigma = 0.3 h^{-1}$ Mpc. The distributions for $\delta_s = -0.5, 0,$ and 1 have maxima at nearly the same flux level ($F_s = 0.8 - 0.95$ in the right panel), and in redshift-space the $\delta_s = 4$ curve is nearly flat over a wide range of flux, so its maximum is poorly defined. This difference is not surprising, since the $\sigma = 1.0 h^{-1}$ Mpc smoothing scale is larger than the BOSS spectral resolution scale, and smoothing the DM density to this scale therefore loses information that is relevant to predicting the BOSS-resolution flux. We will nonetheless find that the LyMAS scheme with $1.0 h^{-1}$ Mpc DM smoothing outperforms the deterministic scheme with $0.3 h^{-1}$ Mpc smoothing.

As described already in the introduction, the philosophy of LyMAS is to assume that the fluxes along separate lines of sight can be drawn independently from the conditional probability distributions $P(F_s | \delta_s)$, with the flux correlations across lines of sight arising from correlations in the underlying DM

density field (coherent fluctuations in the UV background or the IGM equation-of-state could also produce large scale flux correlations; these effects can be incorporated into LyMAS simulations, but we have not done so here). To compute 2-point flux statistics via LyMAS, we create artificial spectra along each of the DM skewers extracted from the simulation, assigning to each pixel a flux that is randomly drawn from the conditional distribution $P(F_s | \delta_s)$ that we have computed from the hydro simulation and illustrated in Figure 6. The creation of artificial spectra is not strictly necessary for computing these flux statistics; it is effectively a convenient Monte Carlo method of doing the relevant integrals over the probability distributions. As discussed in §4 below, the artificial spectra created in this simple manner are unrealistic because they ignore additional correlations (beyond those from DM alone) that arise in neighboring pixels along a single line of sight. In §4 we present a method for creating realistic artificial spectra that have the correct degree of coherence along individual lines of sight, but this more complex method is not needed for predicting flux statistics in the idealized case, with no contribution from observational effects such as noise and continuum fitting errors.

Figure 7 plots conditional PDFs for fluxes of pixels at the identical redshift along lines of sight with transverse comoving separation of $2 h^{-1}$ Mpc: $P(F_1 | F_2, dr, dz)$ is the probability of finding flux F_1 given that the pixel at $dr = 2 h^{-1}$ Mpc,

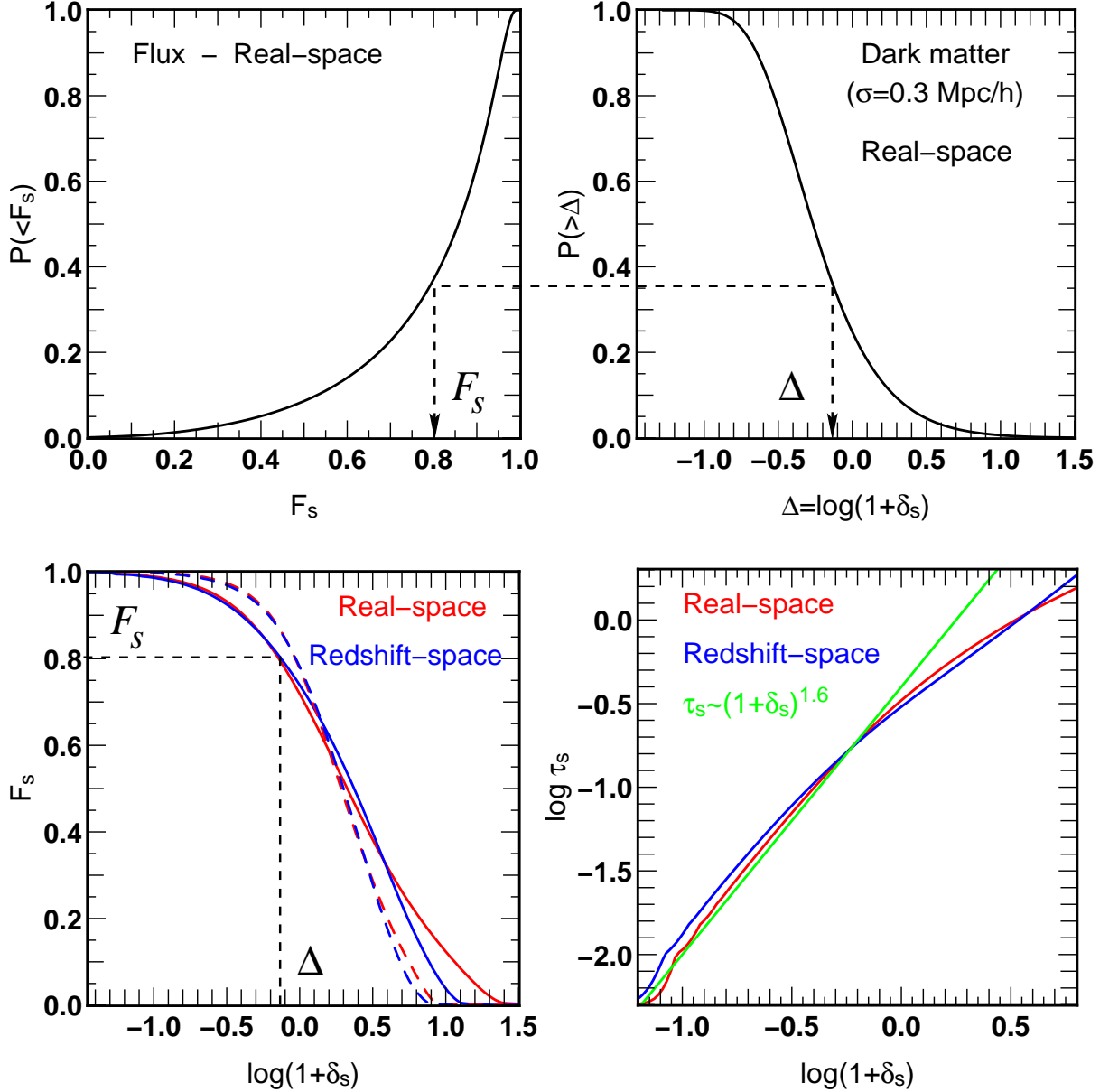


FIG. 5.— Summary of the procedure to get deterministic relations $F(\delta)$. Upper panels plot the cumulative distributions of F_s (left) and δ_s (right). We match a flux F_s to the density contrast δ_s at the same location on the cumulative distribution, with higher fluxes (lower absorption) matched to lower densities. The lower left panel shows the resulting $F_s(\delta_s)$ relations computed in real and redshift space (blue and red solid curves, respectively). Solid lines show results for DM smoothing length $\sigma = 0.3 h^{-1}$ Mpc and dashed lines show results for $1.0 h^{-1}$ Mpc. In the lower right panel we plot $\tau_s = -\ln F_s$ against overdensity $(1 + \delta_s)$ for the $\sigma = 0.3 h^{-1}$ Mpc case. The green line shows the logarithmic slope predicted by the FGPA.

$dz = 0$ has flux $F_2 = 0.2$ (top panels) or 0.6 (bottom panels). In practice, we compute these distributions for pixels with $F_2 = 0.2 \pm 0.005$ or 0.6 ± 0.005 . Left panels show the case with spectra and DM densities both computed in real space (i.e., with all peculiar velocities set to zero), and right panels show the case with both spectra and density fields computed in redshift space. In each panel, the solid black curve shows the unconditional 1-point PDF. As expected, imposing the condition $F_2 = 0.2$, i.e., strong absorption along the neighboring line of sight, increases the probability of F_1 being low. The peak of the conditional distribution is depressed in amplitude, but it is only slightly shifted in location relative to the unconditional PDF. Interestingly, the impact of the F_2

condition is stronger in redshift space than in real space, presumably reflecting the additional effects of coherence in the velocity field. For $F_2 = 0.6$, which still represents fairly strong absorption (about 15th-percentile in the cumulative distribution), we see similar effects but reduced in magnitude.

Even for this fairly small transverse separation, the LyMAS scheme with $\sigma = 0.3 h^{-1}$ Mpc reproduces the results from the true hydro spectra⁸ almost perfectly, with the most noticeable error being a small deviation in the height of the peak. The deterministic scheme is considerably less accurate, especially in redshift space and for the lower F_2 . Remarkably,

⁸ We hereafter refer “true hydro spectra” or “true spectra” to as spectra derived from the MareNostrum hydro simulation.

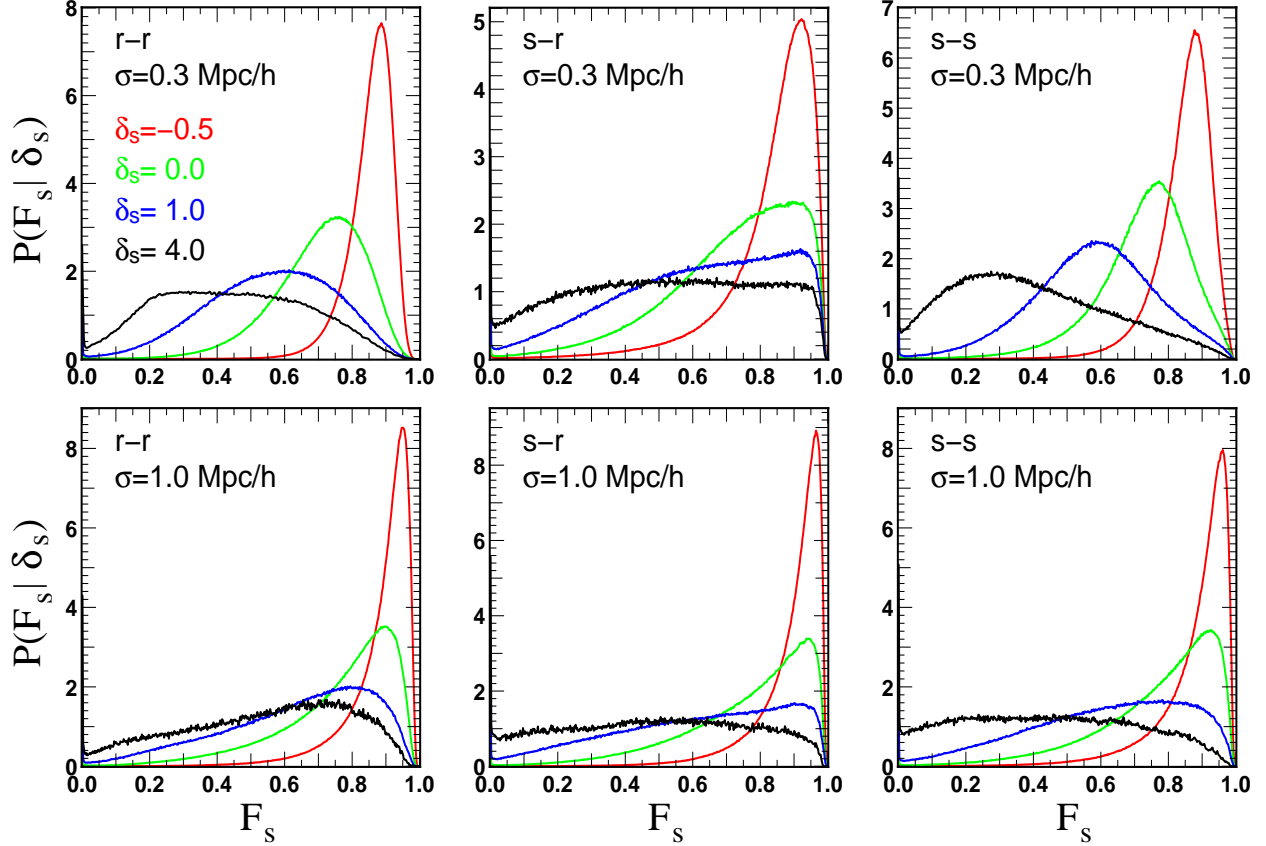


FIG. 6.— Conditional probability distributions $P(F_s|\delta_s)$ for the smoothed flux at different values of the density contrast $\delta_s = -0.5, 0.0, 1.0,$ and 4.0 , as labeled. Upper and lower panels correspond to DM smoothing lengths $\sigma = 0.3 h^{-1} \text{ Mpc}$ and $1.0 h^{-1} \text{ Mpc}$, respectively. Left panels are in real space, right panels are in redshift space, and middle panels use redshift-space spectra but real-space DM densities.

despite the broader conditional distributions seen in Figure 6, LyMAS with $\sigma = 1.0 h^{-1} \text{ Mpc}$ is nearly as accurate as with $\sigma = 0.3 h^{-1} \text{ Mpc}$ when computing the conditional flux PDF at these separations, and it is again much more accurate than the deterministic relation. The blue-dashed curve in all panels shows results for the “coherent” pseudo-spectrum method described in §4; for now, we simply note that they are essentially identical to those from our “minimal” LyMAS scheme with the same DM smoothing length. Grey curves in the right panels show the effect of using the real-space DM density to predict the redshift-space flux. The performance is much worse than using the redshift-space density field, as expected given our previous results. For all future plots, we will use only the redshift-space hydro spectra and the redshift-space DM density fields.

We note that all four of the schemes shown in Figure 7 reproduce the unconditional 1-point PDF of the true spectra by construction, up to tiny statistical fluctuations associated with the finite number of spectra that we have created.

Figure 8 presents a broader view of the conditional flux distributions. We now consider three different transverse separations, $dr = 1, 2,$ and $5 h^{-1} \text{ Mpc}$, and four different conditioning flux values, $F_2 = 0.2, 0.4, 0.6,$ and 0.8 . Two of the panels in the middle column repeat the two right-hand panels of Figure 7. We can see a number of trends, all in qualitative agreement with expectations. The impact of the conditioning flux is strongest when the transverse separation is small, though it is still noticeable at $dr = 5 h^{-1} \text{ Mpc}$. As the condi-

tioning flux F_2 is increased, the conditional PDF of F_1 shifts towards higher flux values. For $F_2 = 0.8$ and $dr = 5 h^{-1} \text{ Mpc}$, the conditional PDF nearly matches the unconditional PDF. LyMAS predictions are more accurate than those from the deterministic scheme in every case, though the difference becomes smaller as the conditional PDF approaches the unconditional PDF. For $\sigma = 0.3 h^{-1} \text{ Mpc}$, LyMAS is impressively accurate even for a transverse separation $dr = 1 h^{-1} \text{ Mpc}$. For $\sigma = 1.0 h^{-1} \text{ Mpc}$, the predictions are noticeably less accurate at $dr = 1 h^{-1} \text{ Mpc}$ than at $dr = 2 h^{-1} \text{ Mpc}$, though still much more accurate than those of the deterministic scheme. The coherent spectrum method of §4 gives results that are essentially indistinguishable from those of the minimal LyMAS in all cases.

Conditional distributions like those in Figure 8 provide a comprehensive description of the two-point correlations in the Ly α F flux field. However, they are difficult to measure from spectra with significant noise, since the underlying flux PDFs are convolved with the noise distribution. Figure 9 shows a higher-level summary statistic, the conditional mean flux $\langle F_1 \rangle = \int_0^1 F_1' P(F_1'|F_2, dr, dz) dF_1'$, plotted as a function of transverse separation dr for various choices of the conditioning flux F_2 . The effects of noise on the PDF of F_1 should average to zero when computing the conditional mean, making this a more easily measurable statistic (it also requires fewer lines of sight to give a useful measurement). However, a proper comparison to observations would have to account for the effects of noise on the conditioning flux F_2 , which do *not* cancel by

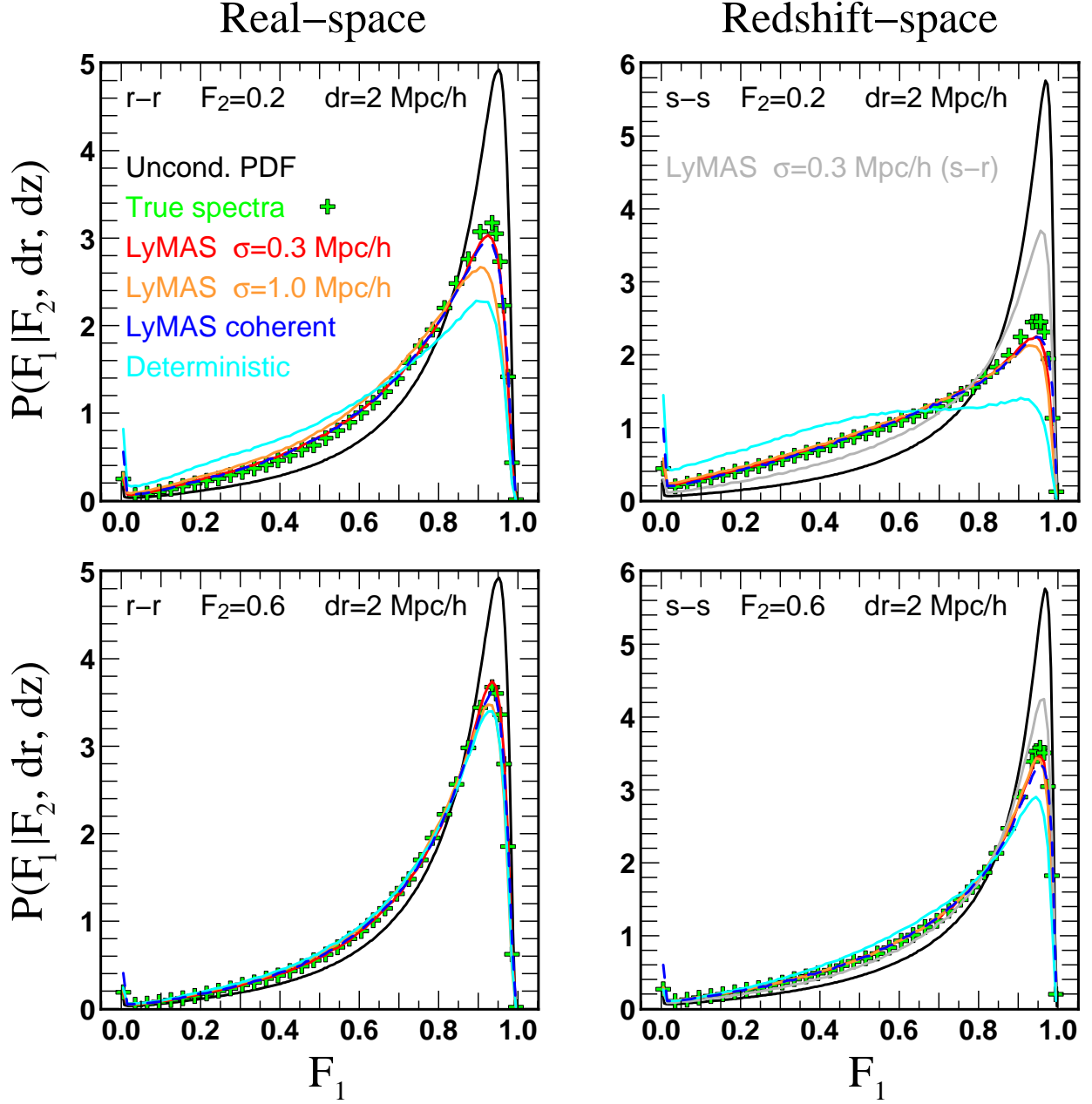


FIG. 7.— Two-point conditional flux PDF $P(F_1|F_2, dr, dz)$ computed for $dr = 2.0h^{-1}$ Mpc and $dz = 0$, computed in real space (left panels) and redshift space (right panels). Upper and lower panels show conditioning flux $F_2 = 0.2 \pm 0.005$ or 0.6 ± 0.005 , respectively. In each panel we show the conditional PDF for the true hydro spectra (green crosses), LyMAS results for DM smoothing $\sigma = 0.3h^{-1}$ Mpc (red) and $1.0h^{-1}$ Mpc (orange), and results for the deterministic method with $\sigma = 0.3h^{-1}$ Mpc (cyan). Black curves show the unconditional PDF for comparison. Blue dashed curves, which are nearly indistinguishable from the red curves, show results from the “coherent” LyMAS scheme described in §4. In the right panels, grey curves show the result of using the real-space DM density field to predict the redshift-space spectra.

averaging; we ignore these effects here. Note that the vertical scales are different in each panel. As expected, the conditional mean flux approaches the unconditional mean $\bar{F} = 0.796$ at large dr , and it dips (or, in the case of $F_2 = 0.9$, rises) towards the value of F_2 for small transverse separation. Starting from the value at $dr = 0.5h^{-1}$ Mpc, the conditional mean has typically recovered about halfway towards the unconditional value by $dr = 3h^{-1}$ Mpc. LyMAS with $\sigma = 0.3h^{-1}$ Mpc reproduces the results from the true hydro spectra accurately in all cases even down to $dr = 0.5h^{-1}$ Mpc. It is substantially more accurate than the deterministic scheme, which

tends to strongly overestimate the impact of the F_2 condition at small transverse separations. With the finer discrimination allowed by this summary statistic, we see that the $\sigma = 1.0h^{-1}$ Mpc smoothing length makes LyMAS noticeably less accurate even at separations of $6-8h^{-1}$ Mpc, though the largest discrepancy arises at $dr \leq 1h^{-1}$ Mpc, and even with the larger smoothing length LyMAS is almost always more accurate than the deterministic scheme computed with the optimal smoothing length.

Finally, Figure 10 shows the variations in redshift space of the correlation function $\xi(s, \mu) = \langle F_1(r, z)F_2(r + dr, z +$

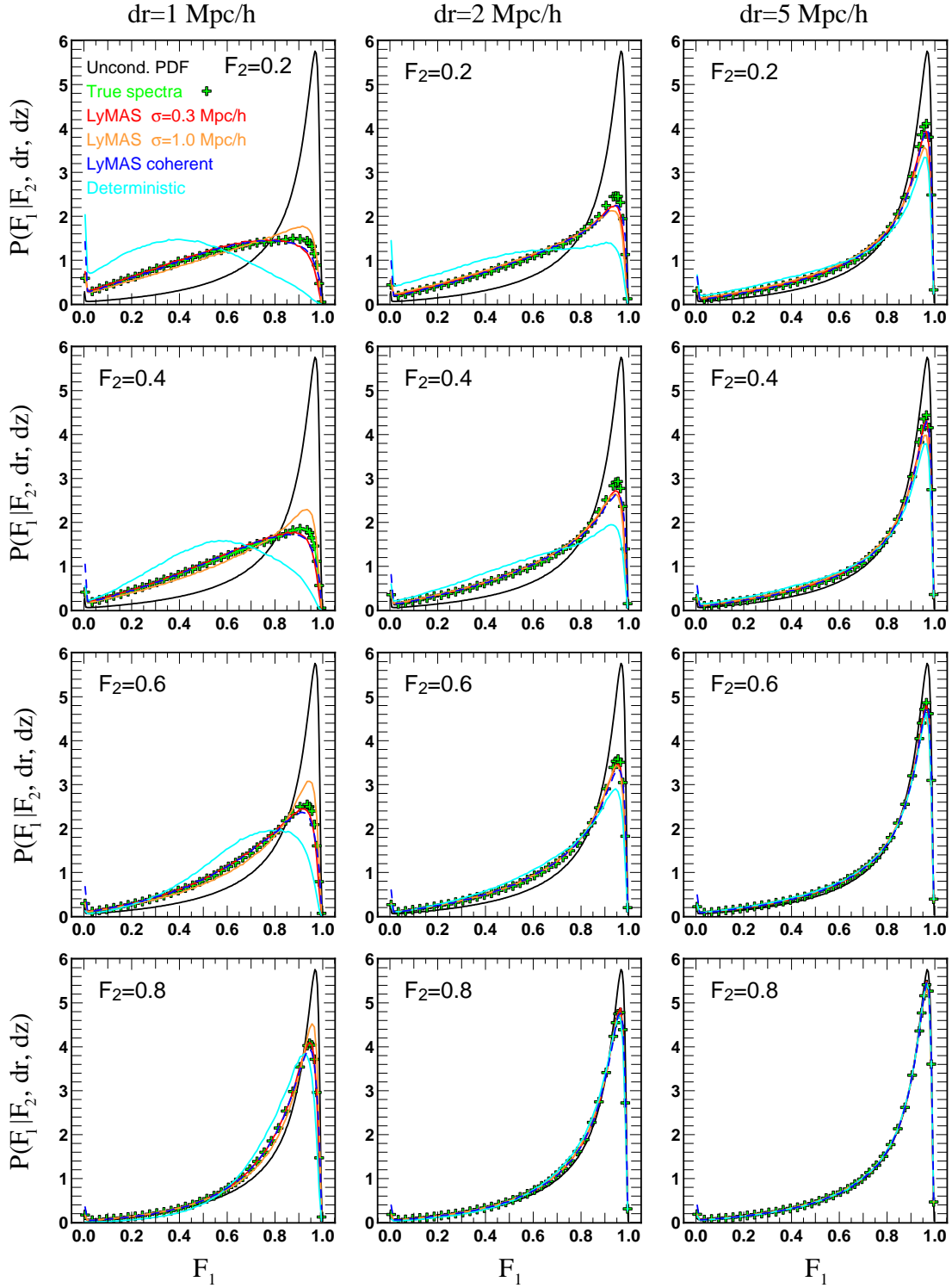


FIG. 8.— Two-point conditional flux PDF, plotted as in Fig. 7 but for a wider range of separations and conditioning flux values, with all computations in redshift space. Left, middle, and right columns show transverse separations $dr = 1.0, 2.0,$ and $5.0 h^{-1} \text{ Mpc}$, respectively, with $dz = 0$ in all cases. Rows from top to bottom show conditioning flux $F_2 = 0.2, 0.4, 0.6,$ and 0.8 .

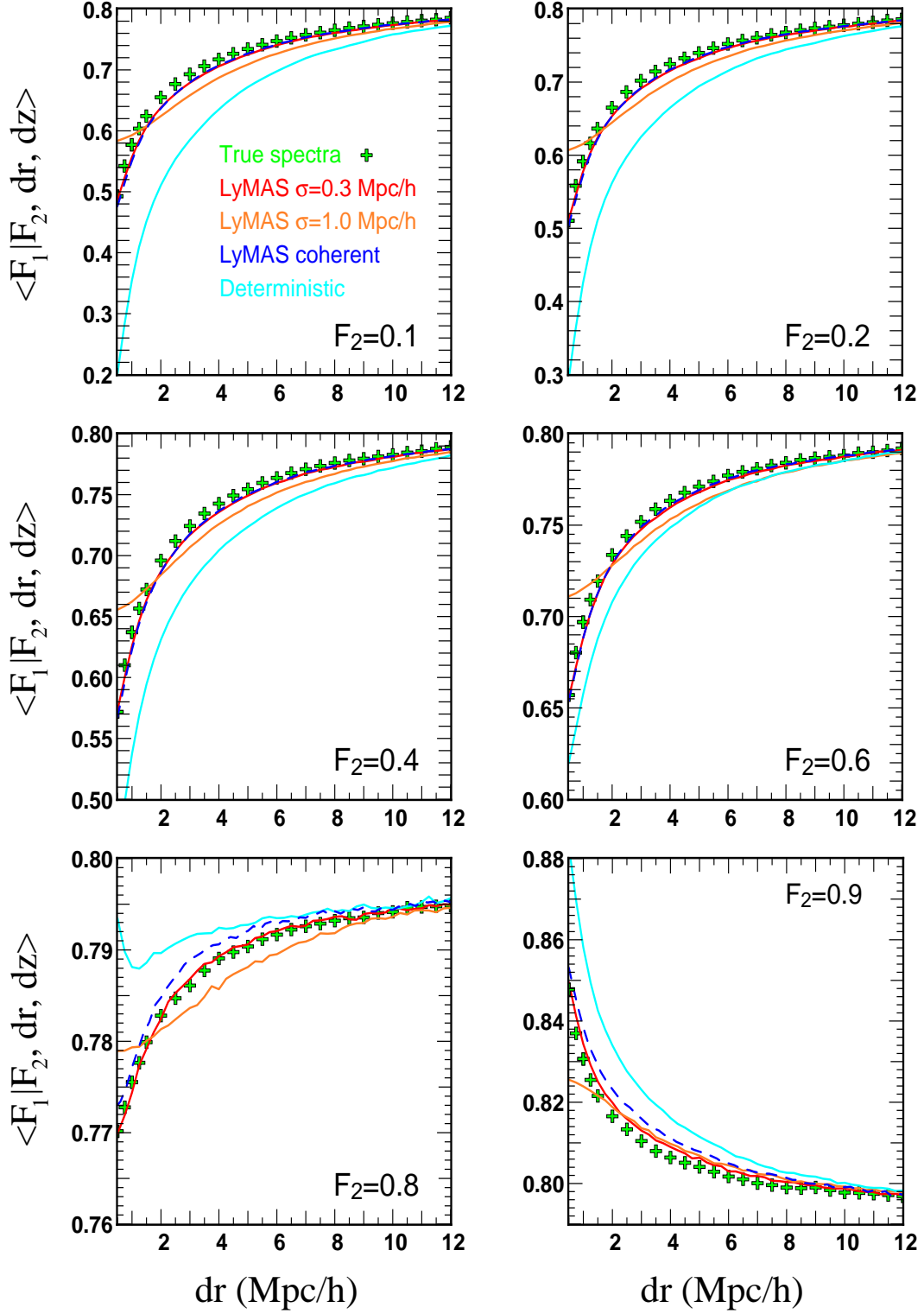


FIG. 9.— The conditional mean flux $\langle F_1 | F_2, dr, dz \rangle$ as a function of transverse separation dr (with $dz = 0$), for six values of F_2 as labeled. We again show results from the true hydro spectra as green crosses, with curves showing results from LyMAS with $\sigma = 0.3 h^{-1}$ Mpc (red) or $1.0 h^{-1}$ Mpc (orange) or the deterministic method with $\sigma = 0.3 h^{-1}$ Mpc (cyan). Blue dashed curves, virtually indistinguishable from the red curves, show results from the coherent LyMAS scheme described in §4. All computations are in redshift space.

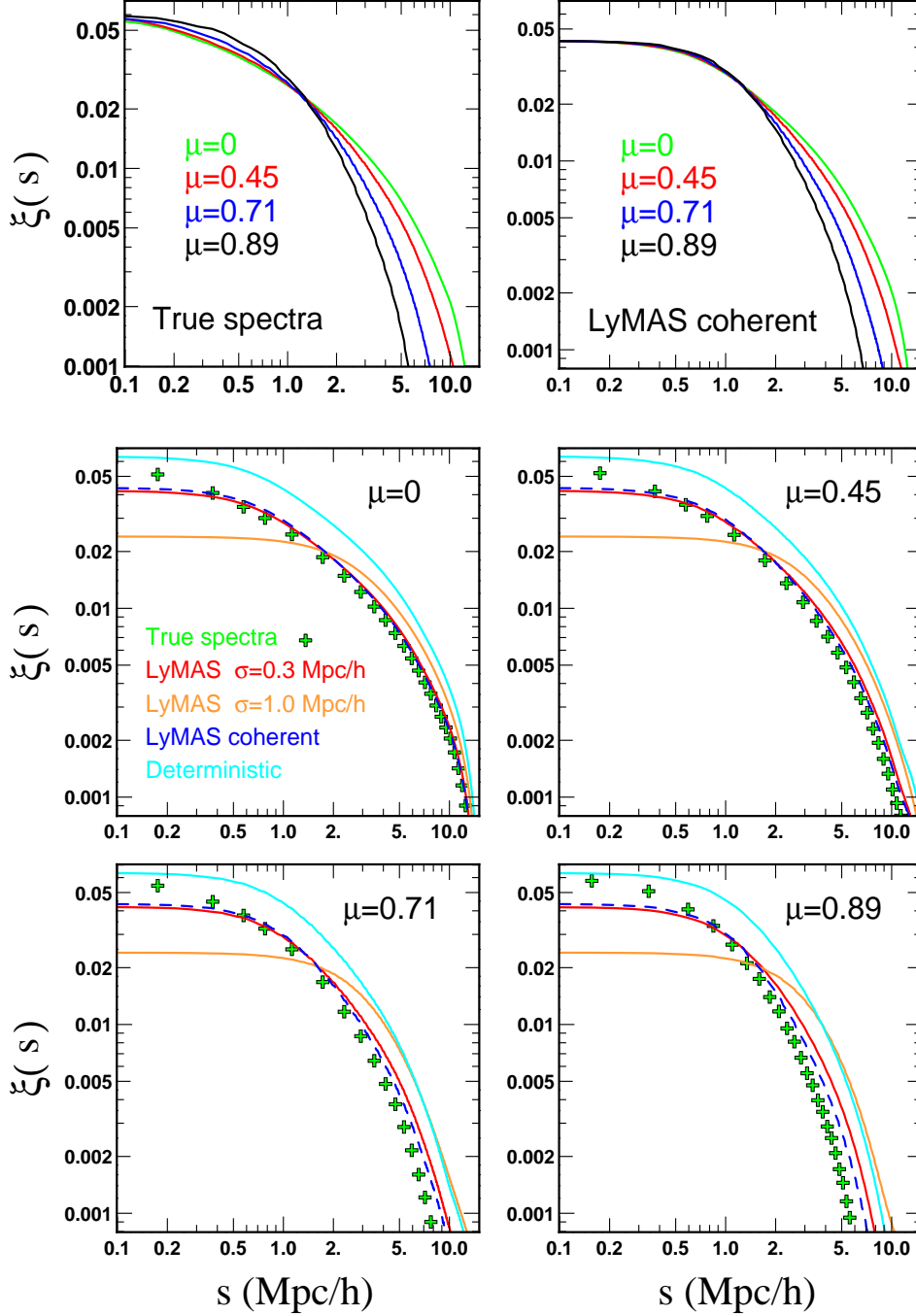


FIG. 10.— The correlation function $\xi = \langle F_1(r, z)F_2(r + dr, z + dz) \rangle / \langle F \rangle^2 - 1$ as a function of the separation $s = (dr^2 + dz^2)^{1/2}$, for four angles: $dz = 0$ ($\mu = 0$), $dr = 0.5dz$ ($\mu \simeq 0.45$), $dr = dz$ ($\mu \simeq 0.71$) and $dr = 2dz$ ($\mu \simeq 0.89$). Again, we present results from the true hydro spectra as green crosses, with curves showing results from LyMAS with $\sigma = 0.3h^{-1}$ Mpc (red) or $1.0h^{-1}$ Mpc (orange) or the deterministic method with $\sigma = 0.3h^{-1}$ Mpc (cyan). Blue dashed curves show results from the coherent LyMAS scheme described in §4. All computations are in redshift space. Top panels show all four μ values on a single plot for the true spectra (left) and coherent LyMAS with $\sigma = 0.3h^{-1}$ Mpc (right).

dz) / $\langle F \rangle^2 - 1$ as a function of the separation $s = (dr^2 + dz^2)^{1/2}$ and angle μ defined for a pair of pixels (i, j) by $\mu = (r_i - r_j)_\parallel / r$, where $r = |r_i - r_j|$ and $(r_i - r_j)_\parallel$ the component along the line of sight. In the present case, we have considered four distinct angles: $dz = 0$ (i.e. $\mu = 0$), $dr = 0.5dz$ ($\mu \simeq 0.45$), $dr = dz$ ($\mu \simeq 0.71$) and $dr = 2dz$ ($\mu \simeq 0.89$). Again, we find that results obtained from the coherent LyMAS scheme with $\sigma = 0.3h^{-1}$ Mpc are in good agreement with those from

the true hydro spectra apart from very small separations ($s \lesssim 0.5h^{-1}$ Mpc) where LyMAS tends to underestimate the correlation function computed from the true spectra. As shown in the top panels, the μ -dependence of $\xi(s, \mu)$ is quite strong, the signature of redshift-space distortions in the Ly α forest. This effect is seen in the observational analysis of BOSS spectra by Slosar et al. (2011). With $\sigma = 0.3h^{-1}$ Mpc, LyMAS predicts this redshift-space distortion accurately, though it performs

somewhat worse at high values of μ . With $\sigma = 1.0 h^{-1} \text{Mpc}$, LyMAS overpredicts $\xi(s, \mu)$ at large μ and $s > 2 h^{-1} \text{Mpc}$, though it outperforms the deterministic scheme for $\mu < 0.5$. It is perhaps somewhat surprising that the discrepancy persists at large s , a point that would be useful to revisit with hydro simulations of a still larger volume. The trends in Figure 10 agree qualitatively with those found by Slosar et al. (2011) in BOSS (their figure 17), but quantitative assessment will require reproducing the continuum removal method of Slosar et al., and it probably requires a larger box to accurately represent large scale flows.

4. CREATING PSEUDO-SPECTRA

As presented in §3, LyMAS is a tool for predicting flux statistics from a dark matter distribution, not for creating realistic artificial Ly α F spectra. However, it is often useful to create such artificial spectra so that one can assess the impact of noise, continuum fitting errors, and other aspects of the observational analysis, and incorporate any biases from these effects into the model predictions before comparing to observations. In this Section we develop a method for creating “pseudo-spectra” with realistic line of sight properties that also have accurate large-scale, 3-d correlations like those predicted by LyMAS.

Figure 11 illustrates the challenge. In the upper panel, the black curve shows the true Ly α F spectrum along a line of sight through the hydro simulation. The red curve shows the result of taking a skewer through the smoothed DM density field along the same line of sight, then drawing flux values at each pixel from our calibrated conditional distribution $P(F_s | \delta_s)$. This curve is much “noisier” than the true spectrum because the LyMAS assumption that separate pixels are represented by *independent* draws from this conditional distribution obviously breaks down when we are examining neighboring pixels along the same line of sight. The second panel of Figure 11 demonstrates this point explicitly by plotting the “percentile spectrum”: for each pixel, we plot the fractional position of the flux value in the true hydro spectrum in the cumulative distribution of $P(F_s | \delta_s)$. Specifically, for a pixel with smoothed flux F_s and smoothed redshift-space density δ_s , we plot

$$\text{Per}(F_s, \delta_s) = \int_0^{F_s} P(F'_s | \delta_s) dF'_s. \quad (4)$$

(To truly make this a “percentile” spectrum we should multiply by 100, but we instead retain the more natural normalization so that Per runs from zero to one.) We see from Figure 11 that when one pixel has a high value of $\text{Per}(F_s | \delta_s)$, and thus a high flux relative to the conditional mean expected given the local DM density, then its neighboring pixels also have high values of $\text{Per}(F_s | \delta_s)$. The coherence of the “percentile field” dies away gradually with separation, but independent draws from $P(F_s | \delta_s)$ lose this coherence entirely.

Figure 11 also suggests a strategy for creating more realistic pseudo-spectra: for each skewer $\delta_s(x)$ through the smoothed DM density field (where x represents redshift-space position along the line of sight), first generate a percentile spectrum $\text{Per}(x)$ with the correct statistical properties, then draw the flux in each pixel from the conditional distribution $P(F_s | \delta_s(x))$ at the location in this distribution implied by $\text{Per}(x)$. The dotted curves in Figures 12a and 12b show, respectively, the line of sight autocorrelation function of $\text{Per}(x)$ and its Fourier transform, the 1-d power spectrum, both computed from the full set of 100,000 spectra from the hydro simulation. Here

we have subtracted the mean $\langle \text{Per}(x) \rangle = 0.5$ and divided by the standard deviation $\sigma(\text{Per}(x)) = \left(\frac{1}{2} + \frac{1}{4} - \frac{1}{3}\right)^{-1/2} = 0.6455$ to create a normalized field. The normalized autocorrelation function drops rapidly from 1.0 at zero separation to 0.1 at $x = 2 h^{-1} \text{Mpc}$, then drops slowly towards large separations. The power spectrum is approximately flat from $k = 0.126 h \text{Mpc}^{-1}$ (the fundamental of the box) up to $k \approx 1.3 h \text{Mpc}^{-1}$, then drops rapidly at higher k .

To create percentile spectra, we first Gaussianize $\text{Per}(x)$, applying a monotonic mapping that preserves the rank order of pixel values but imposes a Gaussian 1-point PDF — i.e., we replace $\text{Per}(x)$ with

$$G_{\text{Per}}(x) = y; \quad (2\pi)^{-1/2} \int_{-\infty}^y e^{-z^2/2} dz = \text{Per}(x). \quad (5)$$

Gaussianization was introduced by Weinberg (1992) as a method to map the present-day galaxy density field back to cosmological initial conditions, and it was introduced for Ly α F analysis by Croft et al. (1998). In our case, it ensures that the field $G_{\text{Per}}(x)$ has a Gaussian 1-point PDF, though it does not ensure that $G_{\text{Per}}(x)$ is actually a Gaussian field, which requires all multi-point PDFs to be multi-variate Gaussians. Note that we apply the Gaussian mapping collectively to the full ensemble of percentile spectra extracted from the hydro simulation, not one line of sight at a time. By construction, $G_{\text{Per}}(x)$ has zero mean and unit standard deviation. Solid curves in Figures 12a and 12b show the autocorrelation function and 1-d power spectrum of this Gaussianized percentile field. They differ only moderately from those of $\text{Per}(x)$ itself.

For any dark matter skewer, we can now generate a Gaussian field $g_{\text{Per}}(x)$ with same 1-d power spectrum as $G_{\text{Per}}(x)$ in the usual way, by drawing the real and imaginary parts of each Fourier mode \tilde{g}_k from independent Gaussian distributions with variance $P(k)/2$, enforcing the Hermitian condition $\tilde{g}_k = \tilde{g}_{-k}^*$, and Fourier transforming to get a real-valued field $g_{\text{Per}}(x)$ (We use lower case g to distinguish these realizations of Gaussian fields from the original Gaussianized field G_{Per} derived from the hydro simulation). After generating $g_{\text{Per}}(x)$ fields for an ensemble of skewers, we “de-Gaussianize” them to create a realization $\text{per}(x)$ of a percentile field along each line of sight — i.e., we monotonically map the values of $g_{\text{Per}}(x)$ to match the uniform PDF that by definition describes a percentile field. (We again use lower case to distinguish our realization of $\text{per}(x)$ from the $\text{Per}(x)$ field measured from the hydro simulation.) Finally, we create an actual spectrum along each line of sight by drawing the smoothed flux from $P(F_s | \delta_s)$ at the location in the cumulative PDF implied by the realization $\text{per}(x)$, assigning each pixel the value of $F_s(x)$ satisfying

$$\int_0^{F_s(x)} P(F'_s | \delta_s) dF'_s = (2\pi)^{-1/2} \int_{-\infty}^{g_{\text{Per}}(x)} e^{-z^2/2} dz. \quad (6)$$

This procedure is reasonably successful. The third panel of Figure 11 shows three realizations of spectra from this procedure along the same line of sight, which can be compared to the true spectrum in the top panel. The three realizations differ only in the random number seed used to generate $\text{per}(x)$. In contrast to the red curve in the top panel, these pseudo-spectra all display a coherence similar to that of the true spectrum. In an ensemble of pseudo-spectra, the values of $\text{Per}(x)$ will still be uniformly distributed, and we will therefore sample fairly from $P(F_s | \delta_s)$ despite introducing correlations to our

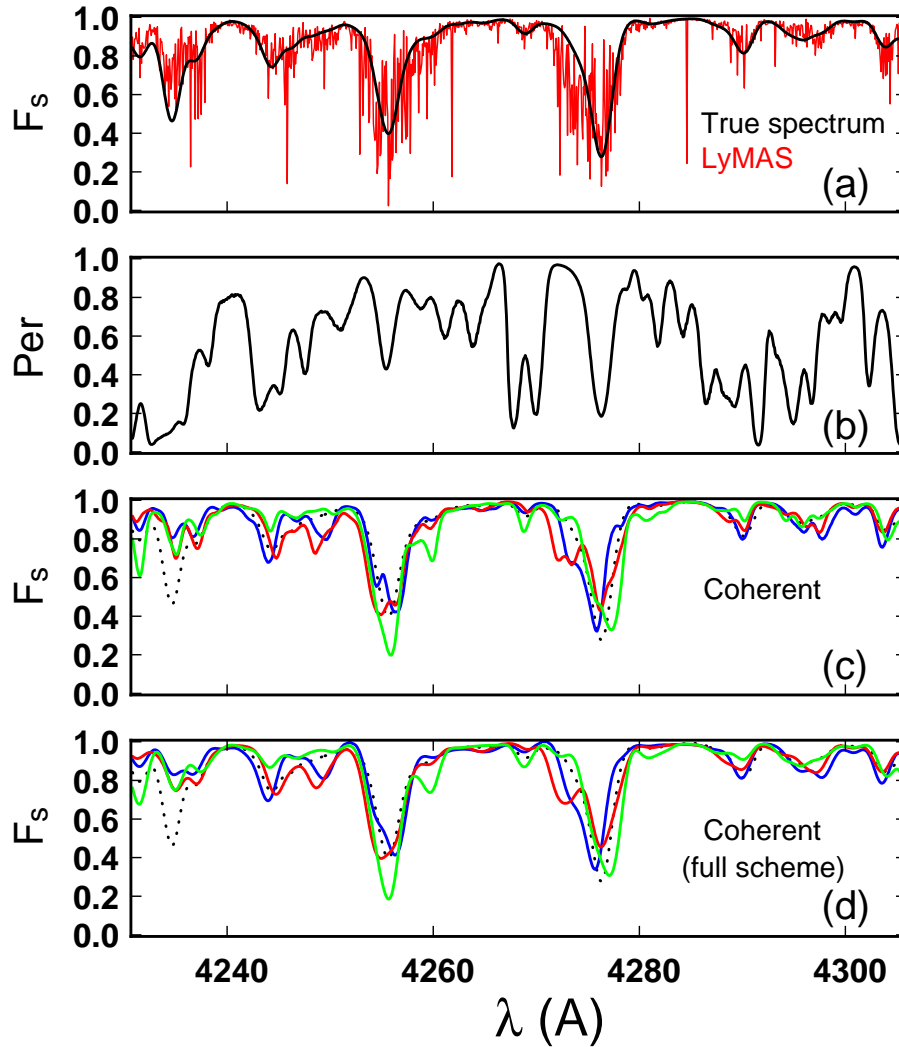


FIG. 11.— (a) True spectrum along a line of sight through the hydro simulation (black) compared to a pseudo-spectrum (red) created by drawing the flux at each pixel independently from the conditional distribution $P(F_s|\delta_s)$. (b) The “percentile spectrum” $\text{Per}(x)$ for this line of sight, showing where in the conditional distribution $P(F_s|\delta_s)$ the value of the flux in the true spectrum lies. (c) Three realizations (with different random number seeds) of a pseudo-spectrum generated from the dark matter skewer along this line of sight, using the scheme described in the text but without the transformation of the 1-d power spectrum and 1-point PDF. The dotted curve shows the true spectrum. (d) The same pseudo-spectra *after* applying the power spectrum and PDF transformations described in the text.

draws for pixels along the same line of sight. By construction, therefore, an ensemble of pseudo-spectra created in this way has the same 1-point PDF as the original hydro spectra and makes the same predictions for the two-point conditional flux PDFs and flux correlation functions as the LyMAS scheme described in §3. (We have confirmed numerically that we do indeed get identical results from the two approaches, up to statistical fluctuations from the finite number of spectra.) We emphasize that this procedure is *not* the same as simply generating Gaussian fields and monotonically mapping them to the flux PDF of the original hydro spectra, as that approach would not use the information in the dark matter skewers along each line of sight and would therefore not build in large scale correlations.

Unfortunately, the 1-d power spectrum of pseudo-spectra generated in this way is not a perfect match to the 1-d power spectrum of the original hydro spectra. Figure 13 shows this comparison, demonstrating that the pseudo-spectra have more

power on small scales and slightly less power on large scales; they are not quite coherent enough. To solve this problem we borrow a scheme from Weinberg & Cole (1992), who were attempting to create non-Gaussian fields with specified power spectra via local transformations of Gaussian fields. In our case, we have a well-defined target power spectrum — that of the ensemble of true hydro spectra — and we have a set of pseudo-spectra whose 1-d power spectrum $P_{F,PS}(k)$ deviates from the target $P_F(k)$, primarily at high k . We repair the discrepancy by computing a 1-d Fourier transform of each pseudo-spectrum, multiplying each Fourier mode by the ratio $[P_F(k)/P_{F,PS}(k)]^{1/2}$, and inverse transforming. The ensemble of modified pseudo-spectra now has the same average 1-d power spectrum as the original hydro spectra, by construction.⁹ As noted by Weinberg & Cole (1992), this power spec-

⁹ We use the values of $P_F(k)$ and $P_{F,PS}(k)$ computed from the ensembles of hydro spectra and pseudo-spectra, so that we do not artificially force the 1-d power spectrum of each individual skewer through the simulation box to

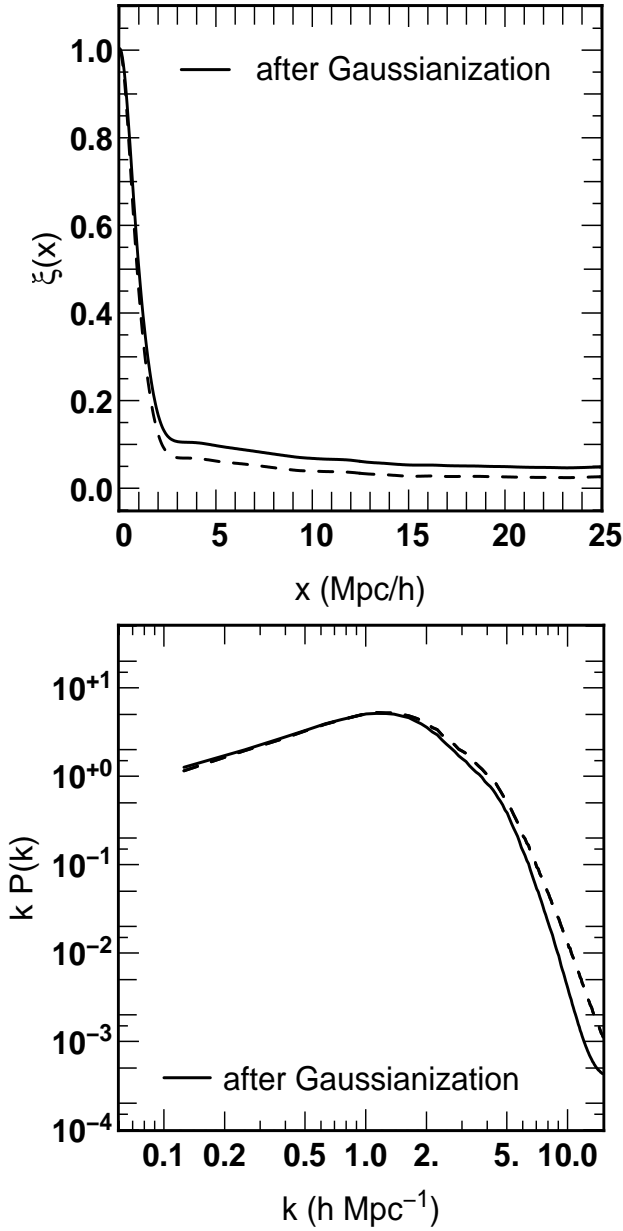


FIG. 12.— (a) Auto-correlation function of the percentile spectra computed from the hydro simulation before (dotted) and after (solid) Gaussianization. (b) dimensionless 1-d power spectra of the same cases. The first mode plotted is the fundamental of the $50h^{-1}$ Mpc box. Both panels show redshift-space results only.

trum modification alters the 1-point PDF, but the change is small. For our purposes, we would like to have spectra that have both the correct 1-d power spectrum and the correct 1-point PDF, and we therefore apply one more monotonic transformation to the fluxes of the pseudo-spectra to match the 1-point PDF of the hydro spectra. This transformation slightly alters the 1-d power spectrum, and in principle one could iterate back and forth between these two steps. In practice, we find that a single iteration already produces excellent agreement with the target 1-d power spectrum up to quite high k , as shown by the dotted curve in Figure 13. The 1-point PDF

match the same global power spectrum.

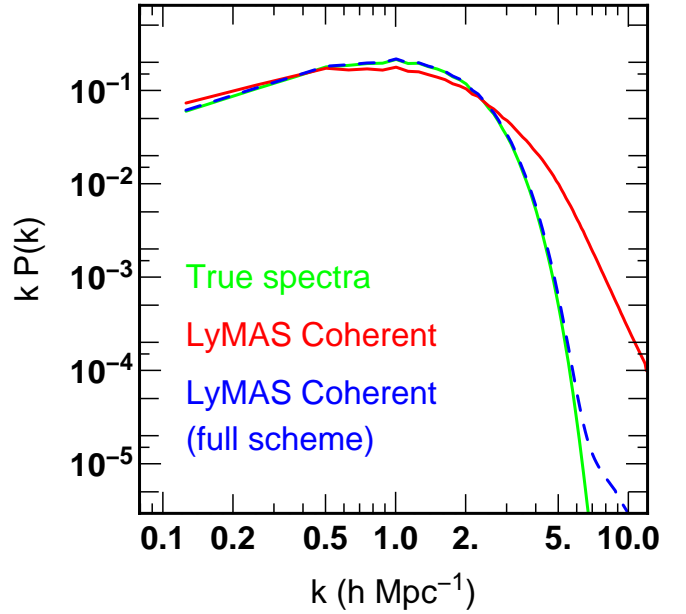


FIG. 13.— Dimensionless 1-d flux power spectrum of the true spectra from the hydro simulation (green), the coherent pseudo-spectra before power spectrum transformation (red), and the pseudo-spectra from our full scheme, after applying the power spectrum and PDF transformations described in the text (blue dashed).

is perfect by construction. We therefore stop after this single iteration. We emphasize that our procedure imposes a global match to the hydro simulation’s flux PDF and 1-d $P(k)$ but does not impose this match spectrum-by-spectrum; each individual spectrum has the expected random fluctuations about the global mean statistics.

In Figures 7-10 we have shown the quantitative predictions of this “coherent” LyMAS scheme with blue dashed curves, and they are almost indistinguishable from those of the simpler procedure described in §3. Therefore, our more elaborate procedure provides a method to create ensembles of pseudo-spectra that have the same 1-d power spectrum and 1-point PDF as those from the hydro simulation and that accurately reproduce the predicted cross-sightline correlations for transverse separations larger than $\sim 1h^{-1}$ Mpc. Note that we have also verified that the coherent scheme with $1.0h^{-1}$ Mpc smoothing generates results similar to the simple scheme with $1.0h^{-1}$ Mpc.

Figure 14 illustrates the relation between the DM density field and the “flux field” $F_{\delta}(\mathbf{x})$ that could in principle be measured on an extremely high density grid of Ly α F sightlines. Upper panels show slices through the density field in real space and redshift space, smoothed with $\sigma = 0.3h^{-1}$ Mpc. Lower panels show the flux field in the same slice computed using the true gas distribution of the hydro simulation, using the deterministic mapping or the simple LyMAS scheme (here labeled “probabilistic”) described in §3, or using the coherent scheme described in this section. It is visually apparent that the true flux field resembles the redshift-space density field more than the real-space density field, as one would expect. In this large scale view, the differences among the three flux assignment schemes are subtle, though one can see that the probabilistic scheme loses some of the fine structure in the true flux field because of its incoherent sampling of $P(F_{\delta}|\delta_{\delta})$.

We close this section with a technical recap of the full Ly-

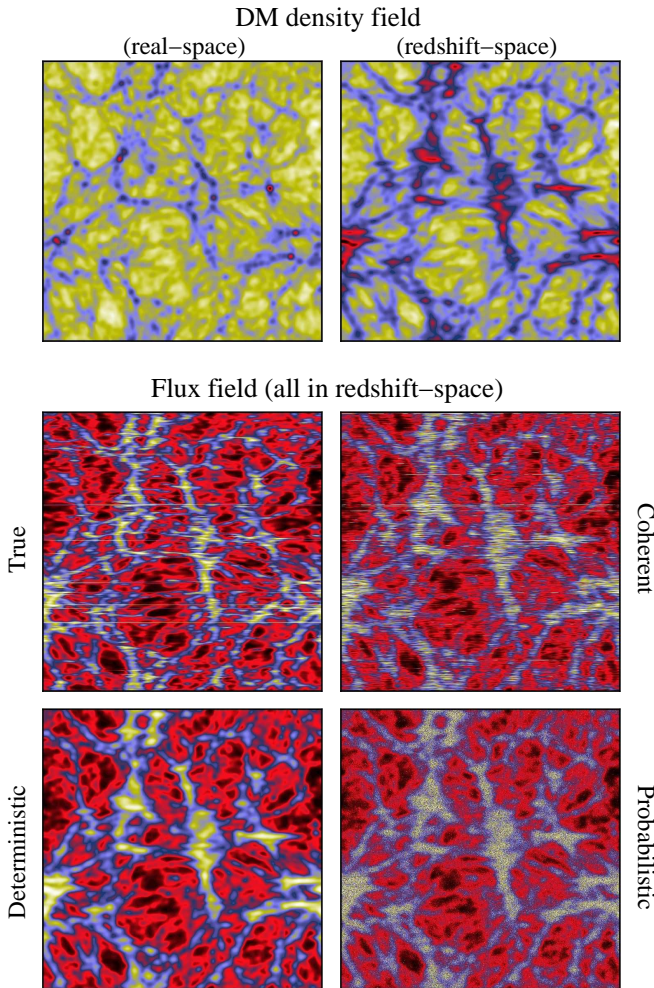


FIG. 14.— Slices through the smoothed DM density field in real space (top left) and redshift space (top right) and through the “flux field” of the true hydro simulation spectra (middle left) and the flux fields created from the $\sigma = 0.3 h^{-1}$ Mpc, redshift-space DM density field using the deterministic mapping (lower left), the probabilistic mapping of §3 (lower right), and the full coherent method described in this section (middle right). The line of sight direction is horizontal in this plot. Yellow colors correspond to low values, while red and dark are high values; the top panels are based on logarithm of density.

MAS recipe for creating an ensemble of pseudo-spectra from a dark matter simulation. The inputs needed from the hydro simulation are:

1. The conditional flux distributions $P(F_s|\delta_s)$ for whatever 3-d smoothing length will be applied to the DM simulation. For BOSS resolution spectra, we find that $\sigma = 0.3 h^{-1}$ Mpc is an optimal choice, but $\sigma = 1.0 h^{-1}$ Mpc still yields good results for transverse separations above $\approx 2 h^{-1}$ Mpc.
2. The 1-d power spectrum and unconditional PDF of the hydro spectra.
3. The 1-d power spectrum of the Gaussianized percentile spectra $G_{\text{per}}(x)$.

In the website dedicated to LyMAS, we provide tabulations of these quantities derived from the RAMSES simulation so that others can use these calibrations to create pseudo-spectra from their own DM simulations.

With these inputs, the steps for creating pseudo-spectra are:

1. Extract skewers through the smoothed DM density field. Our tests in this paper are based on the fairly sophisticated

smoothing scheme described in §2, and we have not tested whether simpler methods give adequate results.

2. For each DM skewer, create a realization $g_{\text{per}}(x)$ of a 1-d Gaussian field with the hydro-calibrated power spectrum of $G_{\text{per}}(x)$. The $P(k)$ computed from our $50 h^{-1}$ Mpc hydro simulation necessarily cuts off at $k = 2\pi/(50 h^{-1} \text{Mpc})$, but the coherence scale of $G_{\text{per}}(x)$ is clearly much smaller than this, about $2 h^{-1}$ Mpc in the autocorrelation function (Fig. 12), so we recommend smoothly truncating the power to zero for the lower k values that arise in large simulations.

3. Along each skewer, create an initial flux field $f_0(x)$ by drawing the flux at each pixel from the location in $P(F_s|\delta_s)$ implied by the value of $g_{\text{per}}(x)$ (eq. 6).

4. Measure the 1-d flux power spectrum $P_{f_0}(k)$ of the ensemble of pseudo-spectra created in this way. Then Fourier transform each pseudo-spectrum, multiply each of its Fourier components by the ratio $[P_F(k)/P_{f_0}(k)]^{1/2}$, and inverse transform to get modified pseudo-spectra $f_1(x)$ that have the same 1-d flux power spectrum $P_F(k)$ as that from the true hydro spectra.

5. Monotonically map the flux values of $f_1(x)$ so that their unconditional PDF matches that of the hydro spectra, obtaining the final realization of the smoothed flux spectra $F_s(x)$.

While one could iterate steps 4 and 5, in our test the final monotonic mapping barely alters the 1-d flux power spectrum, so an iteration is unnecessary. For some purposes, one may prefer pseudo-spectra calibrated to match observations rather than representing the prediction of a theoretical model. In this case, one could use empirical estimates of the flux power spectrum and unconditional PDF in place of the hydro simulation results in steps 4 and 5, while still using the DM simulation to build in realistic large scale flux correlations. One could potentially use an approximate method in place of an N-body simulation to generate the redshift-space DM density field, such as a log-normal transformation of a linear theory, Gaussian realization. One caveat is that this density field will not have the same density PDF as that of the hydro simulation used for calibration, so the pseudo-spectra created in step 3 will not have the correct flux PDF. The results after steps 4 and 5 may still be good, but we have not tested such a case.

5. APPLICATION TO LARGE COSMOLOGICAL DARK MATTER SIMULATIONS

In this section we apply our full LyMAS recipe for creating an ensemble of pseudo-spectra from a large volume dark matter simulation. However, our calibrations of $P(F_s|\delta_s)$ are based on the dark matter distribution of a high-resolution hydro simulation. Two potential complications in applying LyMAS to a larger volume dark matter simulation are that the dark matter in the hydro simulation is affected by gravity of the dissipative baryons and that the PDF of the smoothed dark matter field may be affected by lower resolution. We expect the first effect to be small at the smoothing scales and moderate overdensities relevant to the Ly α forest. To address the resolution question we ran several cosmological N-body simulations with Gadget2 (Springel 2005) with different box lengths and similar cosmological parameters to those used in the MareNostrum simulation. We found that the PDF of the smoothed dark matter density contrast $P(\delta_s)$ agrees well with that from the MareNostrum simulation if the mean inter-particle distance $n_p^{-1/3}$ is similar to the considered smoothing length, as illustrated in Figure 15.

In the following, we analyze two cosmological dark matter

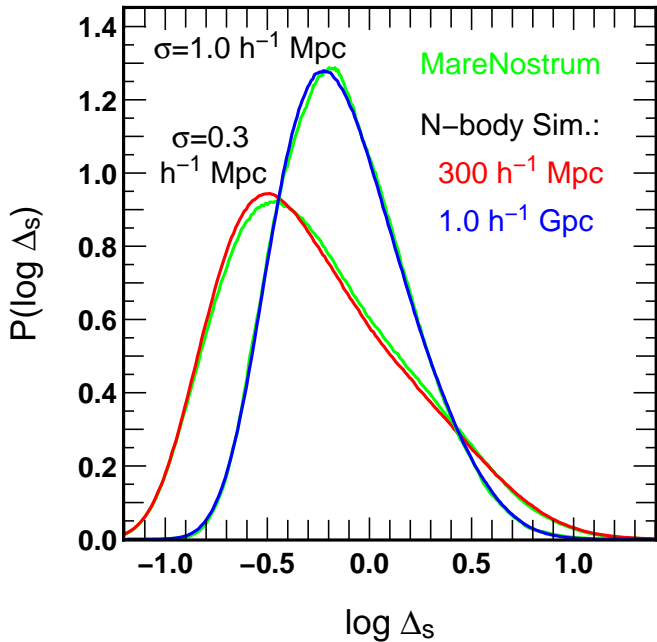


FIG. 15.— Probability distribution functions of $\log \Delta_s$, the logarithm of the smoothed dark matter overdensity, from our 1024^3 Gadget-2 N-body simulations of a $300 h^{-1}$ Mpc box (red) and a $1.0 h^{-1}$ Gpc box (blue), with 3-d smoothing lengths $\sigma = 0.3 h^{-1}$ Mpc and $\sigma = 1.0 h^{-1}$ Mpc, respectively. Green curves show the dark matter overdensity PDFs from the MareNostrum simulation with the same smoothing lengths. All results are at $z = 2.51$.

simulations performed with Gadget2. In order to produce and analyze a reasonable amount of data, each simulation is run with 1024^3 dark matter particles. Thus, to apply our scheme for $\sigma = 1 h^{-1}$ Mpc and $\sigma = 0.3 h^{-1}$ Mpc, appropriate box lengths are respectively $1 h^{-1}$ Gpc and $300 h^{-1}$ Mpc. Initial conditions have been generated using the MPgrafic code (Prunet et al. 2008). The $1 h^{-1}$ Gpc and $300 h^{-1}$ Mpc simulations start at $z = 18.8$ and $z = 30.4$, respectively, and end at $z = 2.51$ where we create our ensembles of pseudo-spectra. In each simulation, the Plummer-equivalent force softening adopted is 5% of the mean inter-particle distance ($48.8 h^{-1}$ kpc and $14.6 h^{-1}$ kpc respectively), kept constant in comoving units. We generate redshift-space dark matter density fields on a 4096^3 grid. While the PDFs of $\Delta_s = 1 + \delta_s$ are already close to those obtained from the hydro simulation (Figure 15), we monotonically remap Δ_s to enforce perfect agreement before generating our pseudo-spectra.

Figure 16 illustrates a pseudo-spectrum through the $1 h^{-1}$ Gpc simulation. The full line of sight has a redshift path length $\Delta z = 1.23$, comfortably larger than the $\Delta z = 0.55$ between the Ly α and Ly β emission lines of a $z = 2.5$ quasar. The lowest, zoomed panel is the same length as a single line of sight through the MareNostrum box, corresponding to an observed-frame wavelength range of 75 \AA . Figure 17 compares the ensemble-average 1-d power spectrum of the MareNostrum hydro spectra and the LyMAS pseudo-spectra from the $300 h^{-1}$ Mpc and $1.0 h^{-1}$ Gpc box. By construction, the power spectra agree essentially perfectly over the common range, with the larger boxes continuing out to lower k . Because we use only a single iteration, there are discrepancies at $k \geq 0.6 h^{-1}$ Mpc, but the power on these scales is too weak to noticeably affect the flux spectra. We have also con-

firmed that the unconditional flux PDFs of the three sets of spectra match perfectly. Figure 18 shows six spectra extracted from the $300 h^{-1}$ Mpc box at $1 h^{-1}$ Mpc intervals of transverse separation. Across a $1 h^{-1}$ Mpc separation, the coherence of structure along neighboring lines of sight is visually evident. By $5 h^{-1}$ Mpc, there is little coherence still obvious to the eye, though flux statistics do reveal correlations at these scales and larger.

The left panel of Figure 19 shows the correlation functions (3-d, redshift-space) of the smoothed dark matter density fields from the MareNostrum simulation and from the $300 h^{-1}$ Mpc and $1.0 h^{-1}$ Gpc N-body simulations. The correlation function of the $50 h^{-1}$ Mpc MareNostrum box is noticeably suppressed at $s = 10 h^{-1}$ Mpc and driven to zero at $s = 16 h^{-1}$ Mpc. The correlation functions of the N-body simulations remain positive to $s \geq 30 h^{-1}$ Mpc. In this plot, the results from the $1.0 h^{-1}$ Gpc simulation should be the most realistic because they are least affected by cutoff of power at the box scale.

The right panel of Figure 19 shows the redshift-space flux correlation function $\xi_F(s)$, averaged over angles and excluding pixel pairs along the same line of sight. The correlation function of the MareNostrum spectra goes negative at $s \approx 16 h^{-1}$ Mpc, reflecting the behavior of the dark matter correlation function in the left panel. The dashed red line in this panel shows the flux correlation function computed from LyMAS pseudo-spectra in the MareNostrum box, with $\sigma = 0.3 h^{-1}$ Mpc. This accurately tracks $\xi(s)$ from the true hydro spectra, as expected based on the previous results in Figure 10. The red curve shows $\xi(s)$ computed by applying LyMAS to the $300 h^{-1}$ Mpc box, again with $\sigma = 0.3 h^{-1}$ Mpc; $\xi(s)$ now remains positive to $s \geq 30 h^{-1}$ Mpc. The blue curve shows $\xi(s)$ from the $1.0 h^{-1}$ Gpc box with $\sigma = 1.0 h^{-1}$ Mpc. While the larger simulation has better representation of large scale power, the predictions are not necessarily more realistic, because $1.0 h^{-1}$ Mpc smoothing yields less accurate results for $\xi(s)$ than $0.3 h^{-1}$ Mpc smoothing (Fig. 10), and the smoothing effect is likely more important than the box size effect on these scales. By contrast, the prediction of the $300 h^{-1}$ Mpc simulation is almost certainly more realistic than that of the MareNostrum simulation, as LyMAS with $\sigma = 0.3 h^{-1}$ Mpc yields accurate predictions of $\xi(s)$ and the box size effects are much weaker for $300 h^{-1}$ Mpc than for $50 h^{-1}$ Mpc.

Dotted and dashed cyan curves in this panel show results from applying the deterministic mapping prescription to the two simulations, with the same smoothing lengths. In each case, the deterministic mapping significantly overpredicts the flux correlation function relative to the more accurate LyMAS scheme, as seen previously for specific μ values in Figure 10. This difference is not surprising, as the stochasticity in the relation between density and flux should suppress the correlation function of the latter with respect to the former. It is important to take these stochastic effects into account when predicting large scale flux correlations from a cosmological model.

Figure 20 plots the flux correlation function averaged in three broad bins of the angle μ , defined as described at the end of Section 3. The amplitude of $\xi_F(s, \mu)$ decreases with increasing μ at fixed s , as seen previously in Figure 10. Comparison of the red lines and the dashed red ones shows the influence of box size between the $50 h^{-1}$ Mpc and $300 h^{-1}$ Mpc simulation volumes. As shown previously in Figure 10, Ly-

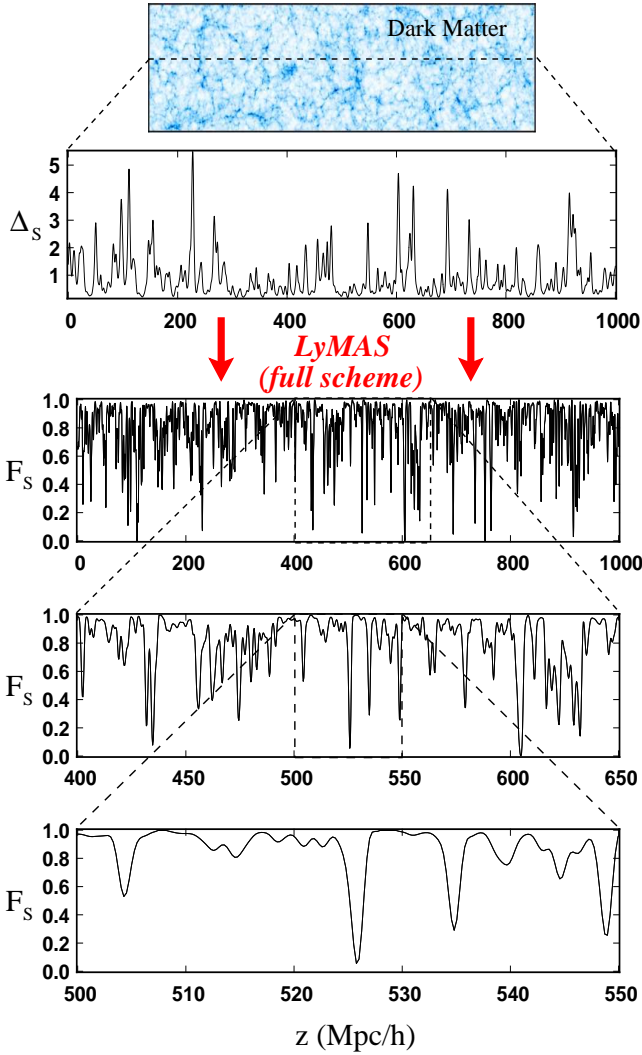


FIG. 16.— Application of the full LyMAS scheme to a large, pure dark matter simulation ($1 h^{-1} \text{ Gpc} - 1024^3$ particles). The second panel plots the dark matter overdensity along the skewer indicated in the top panel, and the three lower panels show successive zooms on the LyMAS pseudo-spectrum, with redshift path lengths (from top to bottom) of $\Delta z = 1.23$, 0.185 , and 0.062 . Equivalently, for the bottom panel, $\Delta\lambda = 75 \text{ \AA}$ and $\Delta v = 5271 \text{ km s}^{-1}$.

MAS is less accurate for high values of μ , indicating some shortcomings at modeling redshift-space distortion for lines of sight with small transverse separations. Nonetheless, the $300 h^{-1} \text{ Mpc}$ box predictions are likely more realistic than those of the MareNostrum hydro spectra because of the larger simulation volume and the good but not perfect accuracy of LyMAS. The higher amplitude correlation function of the $1.0 h^{-1} \text{ Gpc}$ box could be partly due to its larger simulation volume, but comparison to Figure 10 suggests that the dominant effect is the lower accuracy of LyMAS with $1.0 h^{-1} \text{ Mpc}$ smoothing.

Figure 21 shows the conditional mean flux $\langle F_1 | F_2, dr, dz \rangle$ as a function of transverse separation dr (with $dz = 0$), for several values of the conditioning flux F_2 . As shown previously in Figure 9, LyMAS with $\sigma = 0.3 h^{-1} \text{ Mpc}$ reproduces the full hydro predictions for this statistic almost perfectly for $dr \geq 1 h^{-1} \text{ Mpc}$ in the MareNostrum box. The difference between dashed red curves and red curves in the left panel

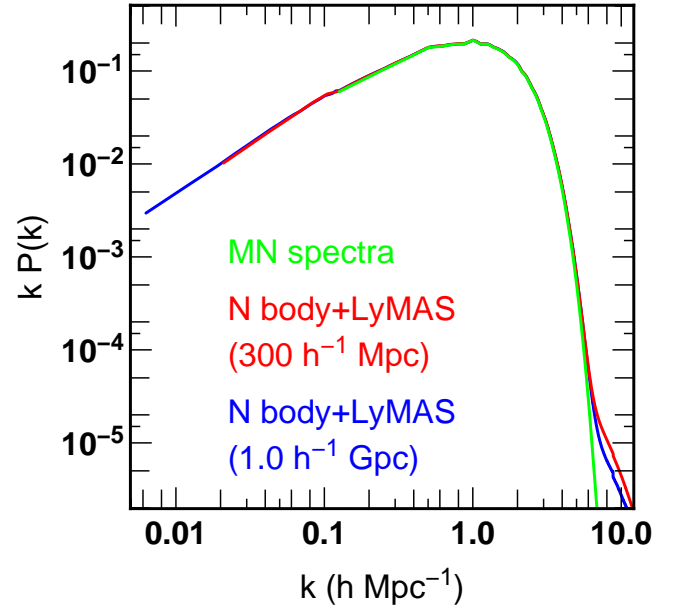


FIG. 17.— The dimensionless, redshift-space, 1-d flux power spectrum of the true spectra from the hydro simulation (green) and coherent pseudo-spectra (full scheme with one iteration) from the $300 h^{-1} \text{ Mpc}$ (red) and $1.0 h^{-1} \text{ Gpc}$ (blue) box side N-body simulations.

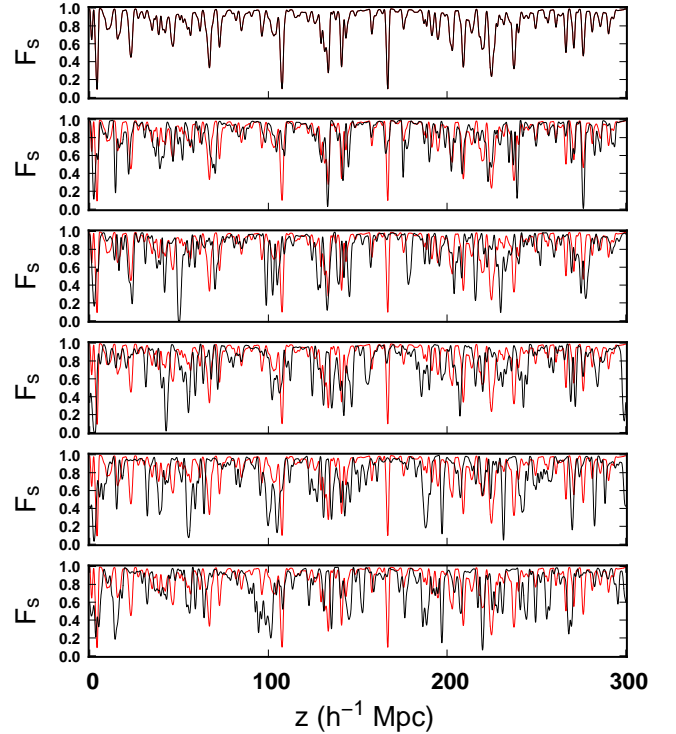


FIG. 18.— Sample of six pseudo-spectra extracted from the $300 h^{-1} \text{ Mpc}$ box simulation along parallel line of sight at $1 h^{-1} \text{ Mpc}$ intervals in transverse separation. The top spectrum is repeated as a red curve in the subsequent panels.

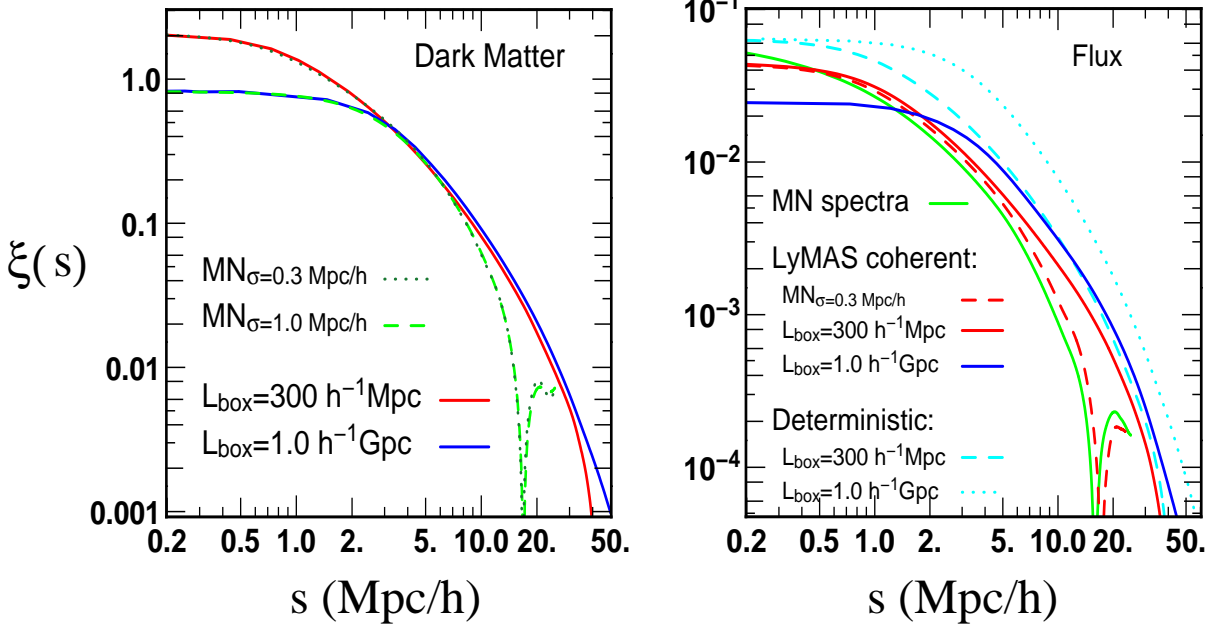


FIG. 19.— (Left) Angle-averaged redshift-space correlation function of the smoothed dark matter density fields, $\xi = \langle \Delta_s(r, z) \Delta_s(r + dr, z + dz) \rangle - 1$, as a function of the separation $s = (dr^2 + dz^2)^{1/2}$, derived from the $50 h^{-1}$ Mpc MareNostrum simulation (dashed and dotted green lines) and the $300 h^{-1}$ Mpc (red) and $1.0 h^{-1}$ Mpc (blue) N-body simulations. The MareNostrum correlation function is negative beyond $s = 16 h^{-1}$ Mpc, a consequence of missing power on scales larger than the box. The smoothing length is $\sigma = 0.3 h^{-1}$ Mpc for MareNostrum (dotted green line) and the $300 h^{-1}$ Mpc box, and $\sigma = 1.0 h^{-1}$ Mpc for MareNostrum (dashed green line) and the $1.0 h^{-1}$ Gpc box. (Right) Angle-averaged redshift-space correlation function of the flux, $\xi_F = \langle F(r, z) F(r + dr, z + dz) \rangle / \langle F \rangle^2 - 1$, for spectra at BOSS resolution. The green curve shows results from the hydro spectra in the MareNostrum simulation. The dashed red curve shows results from LyMAS applied to the MareNostrum dark matter distribution, with $\sigma = 0.3 h^{-1}$ Mpc. Red and blue curves show LyMAS predictions from the $300 h^{-1}$ Mpc and $1.0 h^{-1}$ Gpc simulations with $\sigma = 0.3 h^{-1}$ Mpc and $1.0 h^{-1}$ Mpc, respectively. Dashed and dotted cyan curves show predictions of the deterministic scheme applied to these simulations, with the same smoothing lengths. We consider the red curve to be the most realistic prediction, since it has the high accuracy of the $\sigma = 0.3 h^{-1}$ Mpc LyMAS method but does not suffer from the strong box size effect of the MareNostrum simulation.

therefore reflects the larger box size of the $300 h^{-1}$ Mpc simulation, which noticeably increases the signature of flux correlations on this statistic even for dr as small as $2 - 5 h^{-1}$ Mpc. The right panel shows results from the $1.0 h^{-1}$ Gpc box, but the greater separation between dashed blue and blue curves in this panel likely reflects the lower accuracy of LyMAS with $\sigma = 1.0 h^{-1}$ Mpc (see Fig. 9). Figure 22 shows the conditional mean decrement at separations $dr = 5 - 50 h^{-1}$ Mpc, for the $50 h^{-1}$ Mpc and $300 h^{-1}$ Mpc boxes only. The conditional signal has vanished by $dr = 10 h^{-1}$ Mpc in the MareNostrum spectra, but in the $300 h^{-1}$ Mpc box it continues out to $dr = 25 h^{-1}$ Mpc. Spectra created by deterministic mapping in the $300 h^{-1}$ Mpc box also show this larger scale coherence, but they overpredict the magnitude of the conditional mean effect.

We are making the catalogs of mock spectra from the $300 h^{-1}$ Mpc and $1.0 h^{-1}$ Gpc simulations publicly available¹⁰, as they may be broadly useful for investigating statistics of the 3-d Ly α forest. We also make hydro and LyMAS coherent spectra from the MareNostrum box available so that others can look at the accuracy of LyMAS for statistics they are interested in. These spectra are at $z = 2.51$, and they represent the cosmological model and IGM thermal history used in the MareNostrum simulation. They are smoothed to BOSS spectral resolution, and they are noiseless. We defer the creation of mock spectra that incorporate redshift evolution and noise, and variations of cosmological parameters or IGM parameters, to future work. By construction, these mock

spectra reproduce the 1-d flux power spectrum and flux PDF predicted by the MareNostrum hydro simulation. For predictions of 3-d flux statistics, the spectra from the $300 h^{-1}$ Mpc box should yield similar predictions to those that would be obtained from a RAMSES simulation $(300/50)^3 = 216$ times larger in volume. Predictions from the $1.0 h^{-1}$ Gpc box suffer from the lower accuracy of LyMAS with $\sigma = 1.0 h^{-1}$ Mpc smoothing. Nonetheless, these predictions should be significantly more accurate than those from a deterministic flux mapping scheme, and thus from any previous simulation of the Ly α forest over such a large volume.

6. CONCLUSIONS AND OUTLOOK

LyMAS is a promising method for making accurate predictions for flux statistics of the 3-d Ly α forest on intermediate and large scales. The underlying idea is that flux correlations on these scales are driven by correlations of the dark matter density field, so that flux statistics can be computed by combining the dark matter density field with the conditional PDF of flux given density, $P(F_s | \delta_s)$. Here we have calibrated these conditional PDFs using the $50 h^{-1}$ Mpc MareNostrum AMR hydrodynamic simulation, focusing on spectra matched to the resolution of BOSS at $z \approx 2.5$. We find the tightest flux-density correlation and the best overall performance of LyMAS for a 3-d dark matter smoothing length $\sigma \approx 0.3 h^{-1}$ Mpc (with similar performance down to smaller smoothing lengths of $\sigma \approx 0.2 h^{-1}$ Mpc). The conditional PDFs are quite broad even for this smoothing length, but LyMAS nonetheless gives accurate predictions for the two-point flux

¹⁰ <http://www2.iap.fr/users/peirani/lymas/lymas.htm>

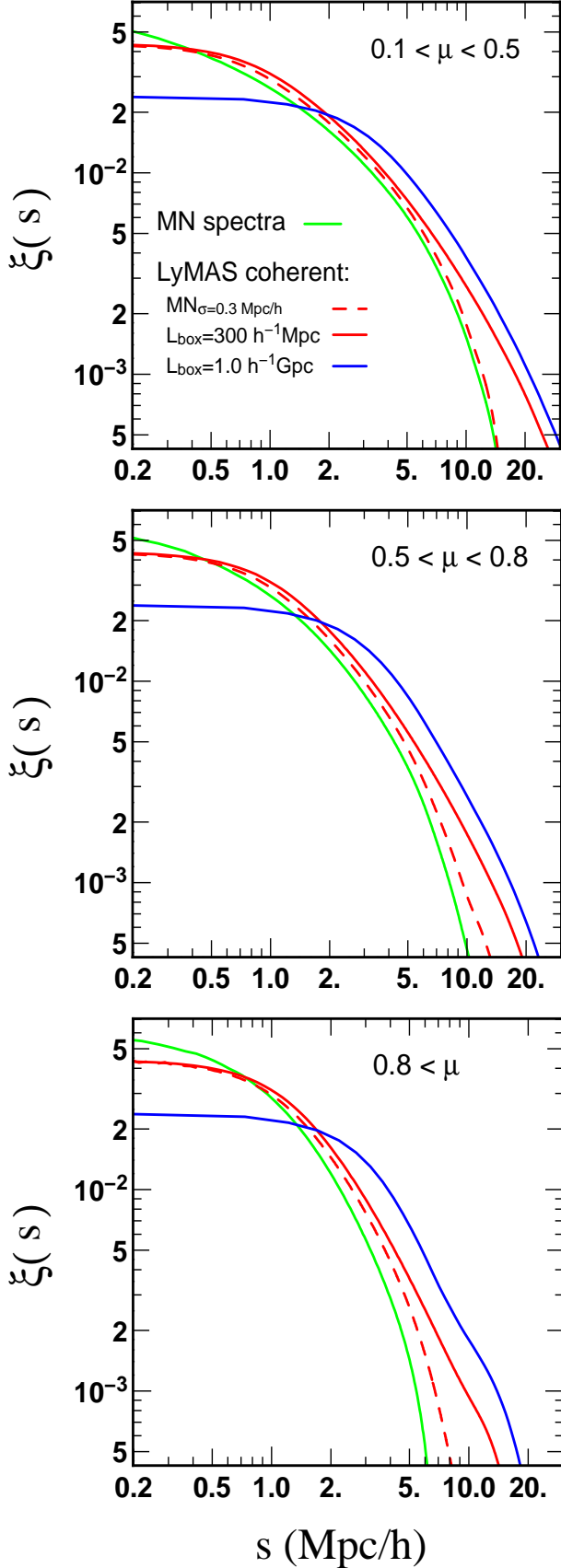


FIG. 20.— Flux correlation functions averaged over bins of angle μ , as labeled. In each panel, green curves show results from the hydro spectra of the MareNostrum simulation, dashed red curves show results from applying LyMAS to the MareNostrum simulation with $\sigma = 0.3 h^{-1}$ Mpc, and red and blue curves show LyMAS results from the $300 h^{-1}$ Mpc box ($\sigma = 0.3 h^{-1}$ Mpc) and the $1.0 h^{-1}$ Gpc box ($\sigma = 1.0 h^{-1}$ Mpc), respectively.

distribution and correlations down to transverse separations as small as $2 h^{-1}$ Mpc. It is substantially more accurate than predictions from a deterministic flux-density mapping, even when the latter is optimally tuned to reproduce the unconditional flux PDF of the hydro simulation. Redshift-space distortions have a different impact on the matter distribution and the Ly α forest, because mass is conserved under the peculiar velocity mapping while absorption is not. Nonetheless, LyMAS predictions for redshift-space flux correlations from the redshift-space dark matter field prove just as accurate as predictions for the real-space flux correlations (i.e., with peculiar velocities set to zero) from the real-space density field.

For forward modeling tests it is desirable to create artificial spectra that can be analyzed with the same procedures applied to observational data. By forming the “percentile fields” described in §4, we are able to make spectra that are coherent from pixel to pixel along a single line of sight and have the same cross-sightline statistics as the simple LyMAS method in which each pixel flux is drawn independently from $P(F_s|\delta_s)$. However, the 1-d flux power spectrum of these coherent spectra has more high- k power than that measured from the full hydro spectra. By remapping first the amplitudes of Fourier modes and then the pixel flux values, as described in §4, we are able to create model spectra that exactly reproduce the 1-d flux power spectrum *and* the unconditional flux PDF of the full hydro spectra. The remapping slightly alters the cross-sightline statistics, but they appear to become, if anything, more accurate in reproducing the full hydro results.

For practical purposes it would be useful to adopt larger dark matter smoothing lengths for large scale predictions, so that LyMAS could be applied to lower resolution dark matter simulations of very large volumes. Unfortunately, LyMAS with $\sigma = 1.0 h^{-1}$ Mpc proves noticeably less accurate than LyMAS with $\sigma = 0.3 h^{-1}$ Mpc even on scales that are much larger than either smoothing length, tending to overpredict the strength of flux correlations. It is still significantly more accurate than a deterministic mapping, even when the latter is applied at $\sigma = 0.3 h^{-1}$ Mpc, so LyMAS remains the best method to make mock Ly α forest spectra from a low resolution N-body simulation. However, $\sigma = 0.3 h^{-1}$ Mpc seems required to achieve the full accuracy of the method, which in turn requires an N-body simulation with $n_p^{-1/3} \lesssim 0.3 h^{-1}$ Mpc. We have not investigated whether a smaller dark matter smoothing length would be needed to model high-resolution spectra (from KECK/UVES for instance). We have also not investigated whether larger smoothing lengths would be acceptable, or even preferred, for modeling spectra with lower resolution than BOSS (X-SHOOTER for instance). But in all cases, one would still need to generate new calibrations $P(F_s|\delta_s)$ and new power spectrum of percentile spectra.

LyMAS shifts the problem of simulating Gpc³ volumes of the Ly α forest from the realm of computationally impossible to computationally challenging. An N-body simulation of a $1 h^{-1}$ Gpc cube with high enough resolution to produce $\sigma = 0.3 h^{-1}$ Mpc dark matter skewers requires $\sim 10^{10}$ particles, and even the creation of the dark matter field from the N-body particle distribution is a cpu- and memory-intensive task. One also requires a calibrating hydrodynamic simulation for each cosmological model of interest, of large enough volume to yield accurate $P(F_s|\delta_s)$. As a first step, we have created catalogs of artificial spectra at BOSS resolution for the MareNostrum cosmology at $z = 2.5$, from a $300 h^{-1}$ Mpc box

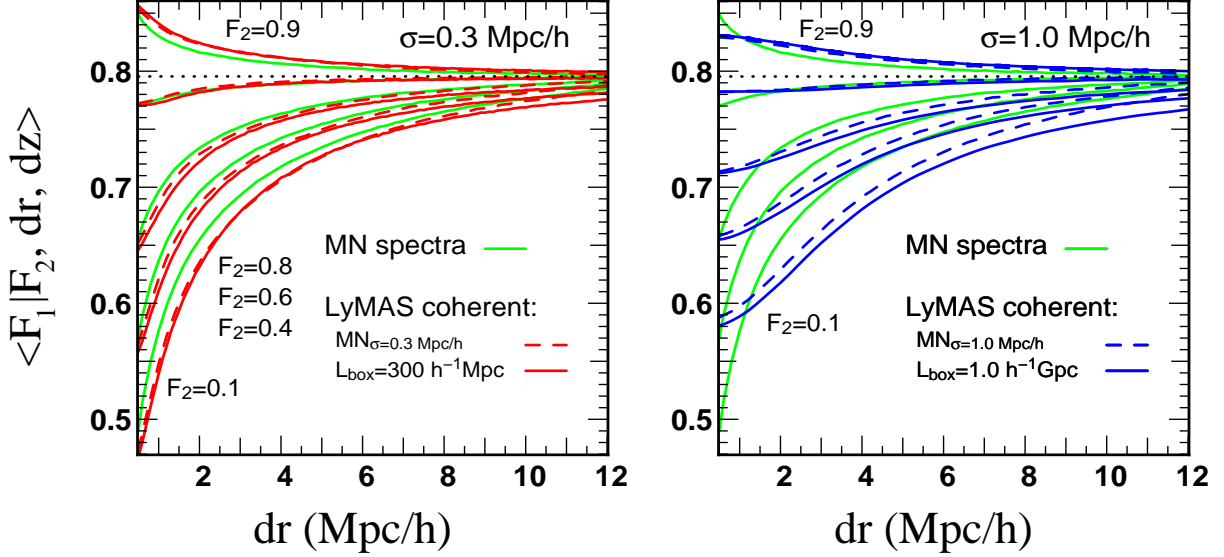


FIG. 21.— Conditional mean flux $\langle F_1|F_2, dr, dz \rangle$ as a function of transverse separation dr (with $dz = 0$), for the labeled values of F_2 . Green curves are derived from the hydro spectra in the $50 h^{-1}$ Mpc MareNostrum box. Dashed red curves and dashed blue curves show results from applying LyMAS to the MareNostrum simulation with $\sigma = 0.3 h^{-1}$ Mpc (left panel) and $\sigma = 1.0 h^{-1}$ Mpc (right panel), respectively. Curves show LyMAS results from the $300 h^{-1}$ Mpc box (left panel, with $\sigma = 0.3 h^{-1}$ Mpc) and the $1.0 h^{-1}$ Gpc box (right panel, with $\sigma = 1.0 h^{-1}$ Mpc).

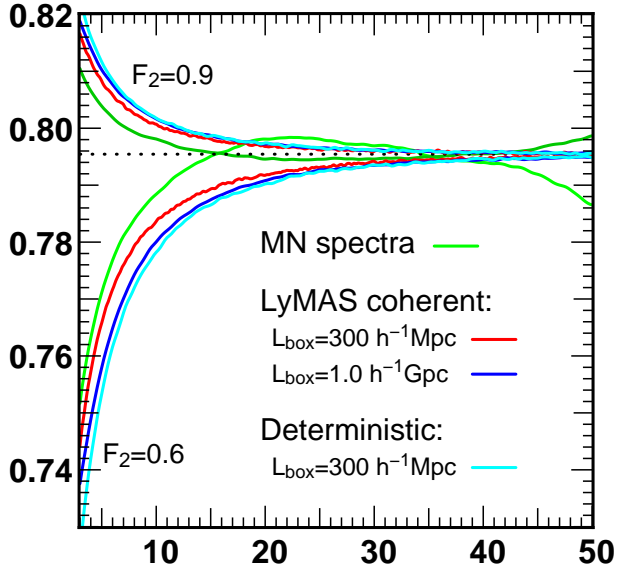


FIG. 22.— Conditional mean flux at larger separation, $dr = 3-50 h^{-1}$ Mpc, for $F_2 = 0.9$ and 0.6 . We show results from the hydro spectra of the MareNostrum box and from LyMAS and deterministic mapping applied to the $300 h^{-1}$ Mpc box with $\sigma = 0.3 h^{-1}$ Mpc.

with $\sigma = 0.3 h^{-1}$ Mpc and a $1 h^{-1}$ Gpc box with $\sigma = 1.0 h^{-1}$ Mpc. In future work, we will investigate methods for incorporating the redshift evolution of the forest over the range probed by an individual quasar spectrum and move towards a full realization (from multiple simulations) of the BOSS quasar sample.

Alongside these technical challenges, the most interesting direction for future study with LyMAS is to explore the sensitivity of medium and large scale structure in the 3-d Ly α forest to the underlying cosmological and IGM parameters. Indeed, if the thermal history of the hydro simulation or the cosmological parameters change, the PDF of the flux and then

the probabilities $P(F_s|\delta_s)$ would also change. At present, we don't know if we still need to derive new calibration tables for each set of specific cosmological parameters (or set of thermal history models) or whether a simple rescaling at some steps from the present study would be acceptable. Nevertheless, These investigations can be started by manipulating the MareNostrum simulation to compute conditional flux PDFs for different IGM equations of state (by artificially changing gas temperatures) or matter fluctuation amplitudes (by relabeling output redshifts), then applying these conditional PDFs to different N-body outputs. These rescaling calculations should be spot-checked against fully self-consistent sets of simulations, but we expect they will provide good guidance to the sensitivity of flux statistics to cosmology and degeneracies with the IGM. There are obvious analogies between the LyMAS approach to modeling the Ly α forest and methods for creating galaxy redshift catalogs by populating the dark matter halos of N-body simulations in accord with semi-analytic models of galaxy formation, with the advantage that predicting the Ly α forest from first principles is more straightforward than modeling galaxy formation. However, the effects of ionizing background fluctuations (Croft 2004), inhomogeneous reionization (McQuinn et al. 2011), and metal-line contamination remain important potential systematics that require further scrutiny.

The potential payoff from exploiting sub-BAO scales in the 3-d Ly α forest is large. One long-recognized opportunity is to apply the Alcock-Paczynski (1979) test to the Ly α forest to constrain the product $H(z)D_A(z)$ at high redshift (Hui, Stebbins, & Burles 1999; McDonald & Miralda-Escudé 1999); this requires accurate predictions of the intrinsic anisotropy in Ly α forest clustering. A more model-dependent variant of this idea is to use the amplitude of correlations as a function of transverse separation to constrain $D_A(z)$ directly. The slope and curvature of the matter power spectrum are diagnostics for neutrino masses or curvature in the inflationary fluctuation spectrum, and the Ly α forest can probe the power spectrum shape on scales that are degraded by non-linear evo-

lution at low redshift. Most enticing but perhaps most challenging is the prospect of precisely constraining the amplitude of matter clustering at $z = 2-4$, so that Λ CDM predictions for the growth of structure can be tested from the CMB epoch through the Ly α forest epoch down to the lower redshifts probed by large weak lensing and galaxy redshift surveys. These tests could reveal the signatures of complex dark energy models or deviations from General Relativity on cosmological scales. With the massively multi-plexed spectroscopic surveys underway and planned for the future, the 3-d Ly α forest is emerging as a major new route to tracing the growth of structure in the universe. LyMAS is an important step towards matching theoretical predictions to this observational opportunity.

DW acknowledges the hospitality of the Institut d’Astrophysique de Paris, support of grant AST-1009505

from the U.S. National Science Foundation, and additional support from French state funds managed by the ANR within the Investissements d’Avenir program under reference ANR-11-IDEX-0004-02. We also acknowledge support from the “Programme National Cosmologie et Galaxies”. This work was carried within the framework of the Horizon project (<http://www.projet-horizon.fr>). Most of the numerical modeling presented here was done on the Horizon cluster at IAP. We warmly thank the referee for his/her useful comments that improved the quality of the original manuscript. We warmly thank T. Sousbie, S. Prunet, S. Rouberol and M. Peebles for stimulating discussions. We also thank D. Munro for freely distributing his Yorick programming language (available at <http://yorick.sourceforge.net/>) which was used during the course of this work.

REFERENCES

- Alcock, C., & Paczyński, B. 1979, *Nature*, 281, 358
 Angulo, R. E., & White, S. D. M. 2010, *MNRAS*, 405, 143
 Bi, H.G., & Davidsen, A. 1997, *ApJ*, 479, 523
 Busca, N. G., Delubac, T., Rich, J., et al. 2013, *A&A*, 552, A96
 Cen, R., Miralda-Escudé, J., Ostriker, J.P., & Rauch, M. 1994, *ApJ*, 437, L9
 Colombi, S., Chodorowski, M. J., & Teyssier, R. 2007, *MNRAS*, 375, 348
 Croft, R. A. C. 2004, *ApJ*, 610, 642
 Croft, R.A.C., Weinberg, D.H., Katz, N., Hernquist, L., 1997, *ApJ*, 488, 532
 Croft, R. A. C., Weinberg, D. H., Katz, N., & Hernquist, L. 1998, *ApJ*, 495, 44
 Croft, R. A. C., Weinberg, D. H., Pettini, M., Katz, N., & Hernquist, L. 1999, *ApJ*, 520, 1
 Croft, R. A. C., Weinberg, D. H., Bolte, M., Burles, S., Hernquist, L., Katz, N., Kirkman, D., Tytler, D. 2002, *ApJ*, 581, 20
 Devriendt, J., Rimes, C., Pichon, C., et al. 2010, *MNRAS*, 403, L84
 Dawson, K. S., Schlegel, D. J., Ahn, C. P., et al. 2013, *AJ*, 145, 10
 Dubois, Y., & Teyssier, R. 2008, *A&A*, 477, 79
 Eisenstein, D. J., Weinberg, D. H., Agol, E., et al. 2011, *AJ*, 142, 72
 Faucher-Giguère, C.-A., Prochaska, J. X., Lidz, A., Hernquist, L., & Zaldarriaga, M. 2008, *ApJ*, 681, 831
 Font-Ribera, A., McDonald, P., & Miralda-Escudé, J. 2012, *JCAP*, 1, 1
 Gallerani, S., Kitaura, F. S., & Ferrara, A. 2011, *MNRAS*, 413, L6
 Gnedin, N. Y., & Hui, L. 1996, *ApJ*, 472, L73
 Gnedin, N. Y., & Hui, L. 1998, *MNRAS*, 296, 44
 Greig, B., Bolton, J. S., & Wyithe, J. S. B. 2011, *MNRAS*, 418, 1980
 Gunn, J.E., & Peterson, B.A. 1965, *ApJ*, 142, 1633
 Haardt, F., & Madau, P. 1996, *ApJ*, 461, 20
 Hernquist L., Katz, N., Weinberg, D.H., & Miralda-Escudé, J. 1996, *ApJ*, 457, L51
 Hui, L., & Gnedin, N. 1997, *MNRAS*, 292, 27
 Hui, L., Gnedin, N., & Zhang, Y. 1997, *ApJ*, 486, 599
 Hui, L., Stebbins, A., & Burles, S. 1999, *ApJ*, 511, 5
 Katz, N., Weinberg D.H., & Hernquist, L. 1996, *ApJS*, 105, 19
 Le Goff, J. M., Magneville, C., Rollinde, E., Peirani, S., et al. 2011, *A&A*, 534, A135
 Lidz, A., Faucher-Giguère, C.-A., Dall’Aglio, A., McQuinn, M., Fechner, C., Zaldarriaga, M., Hernquist, L., & Dutta, S. 2010, *ApJ*, 718, 199
 McDonald, P. 2003, *ApJ*, 585, 34
 McDonald, P. & Miralda-Escudé, J. 1999, *ApJ*, 518, 24
 McDonald, P., Miralda-Escudé, J., Rauch, M., Sargent, W. L. W., Barlow, T. A., Cen, R., & Ostriker, J. P. 2000, *ApJ*, 543, 1
 McDonald, P., et al. 2005, *ApJ*, 635, 761
 McDonald, P., & Eisenstein, D. J. 2007, *Phys. Rev. D*, 76, 063009
 McQuinn, M., Hernquist, L., Lidz, A., & Zaldarriaga, M. 2011, *MNRAS*, 415, 977
 Miralda-Escudé J., Cen R., Ostriker, J.P., & Rauch, M. 1996, *ApJ*, 471, 582
 Miralda-Escudé, J., Rauch, M., Sargent, W.L.W., Barlow, T.A., Weinberg, D.H., Hernquist, L., Katz, N., Cen, R. & Ostriker, J.P. 1998, in Proc. of the 13th IAP Colloquium, Structure and Evolution of the IGM from QSO Absorption Line Systems, eds. P. Petitjean & S. Charlot, (Paris: Nouvelles Frontières), p. 155, astro-ph/9710230
 Monaghan, J. J. 1992, *ARA&A*, 30, 543
 Ocvirk, P., Pichon, C., & Teyssier, R. 2008, *MNRAS*, 390, 1326
 Peebles, M. S., Weinberg, D. H., Davé, R., Fardal, M. A., & Katz, N. 2010, *MNRAS*, 349
 Prunet, S., Pichon, C., Aubert, D., et al. 2008, *ApJS*, 178, 179
 Seljegel, D., et al. 2011, The BigBOSS Experiment, arXiv:1106.1706
 Seljak, U., Makarov, A., McDonald, P., Anderson, S., et al. 2005, *Phys. Rev. D*, 71, 3515
 Slosar, A., Ho, S., White, M., & Louis, T. 2009, *Journal of Cosmology and Astro-Particle Physics*, 10, 19
 Slosar, A., et al. 2011, *JCAP*, 9, 1
 Slosar, A., Iršič, V., Kirkby, D., et al. 2013, *JCAP*, 4, 26
 Smee, S., Gunn, J. E., Uomoto, A., et al. 2012, arXiv:1208.2233
 Sousbie, T., Courtois, H., Bryan, G., & Devriendt, J. 2008, *ApJ*, 678, 569
 Spergel, D. N., Verde, L., Peiris, H. V., et al. 2003, *ApJS*, 148, 175
 Springel, V. 2005, *MNRAS*, 364, 1105
 Teyssier, R. 2002, *A&A*, 385, 337
 Thoul, A. A. & Weinberg, D. H. 1996, *ApJ*, 465, 608
 Viel, M., Matarrese, S., Mo, H. J., Theuns, T., & Haehnelt, M. G. 2002, *MNRAS*, 336, 685
 Viel, M., Haehnelt, M. G., & Springel, V. 2004, *MNRAS*, 354, 684
 Viel, M., Haehnelt, M. G., & Springel, V. 2006, *MNRAS*, 367, 1655
 Viel, M., Haehnelt, M. G., & Springel, V. 2010, *JCAP*, 6, 15
 Weinberg, D. H. 1992, *MNRAS*, 254, 315
 Weinberg, D. H., & Cole, S. 1992, *MNRAS*, 259, 652
 Weinberg, D. H., Katz, N., & Hernquist, L. 1998, in ASP Conference Series 148, Origins, eds. C. E. Woodward, J. M. Shull, & H. Thronson, (ASP: San Francisco), 21, astro-ph/9708213
 Weinberg, D. H., et al. 1999, in Evolution of Large Scale Structure: From Recombination to Garching, eds. A.J. Banday, R. K. Sheth, & L. N. Da Costa, (Twin Press: Vledder NL), 346 astro-ph/9810142
 White, M. 2003, The Davis Meeting On Cosmic Inflation, p. 18, astro-ph/0305474
 White, M., Pope, A., Carlson, J., et al. 2010, *ApJ*, 713, 383
 Zaldarriaga, M., Hui, L., & Tegmark, M. 2001, *ApJ*, 557, 519
 Zhang, Y., Anninos, P., & Norman, M.L. 1995, *ApJ*, 453, L57